A Numerical Study on the Aerodynamics of Freely Falling Planar Ice Crystals

Joseph J. NETTESHEIM

A thesis submitted in partial fulfillment of

the requirements for the degree of

Master of Science

(Atmospheric and Oceanic Sciences)

at the

UNIVERSITY OF WISCONSIN-MADISON

2017

Abstract

A Numerical Study on the Aerodynamics of Freely Falling Planar Ice Crystals

by Joseph J. NETTESHEIM

Fluid flow fields and fall patterns of falling planar ice crystals are studied by numerically solving the unsteady, incompressible Navier-Stokes equations using a commercially available computational fluid dynamics package. The ice crystal movement and orientation are explicitly simulated based on hydrodynamic forces and torques representing the six degrees of freedom. This study extends the current framework by investigating four planar-type ice crystals: crystals with sector-like branches, crystals with broad branches, stellar crystals, and ordinary dendritic crystals. The crystals range from 0.1 – 0.5 mm and 1 – 5 mm in maximum dimension, corresponding to Reynolds number ranges from 0.2 – 384. The results indicate that steady flow fields are generated for flows with Reynolds numbers less than 100; larger plates generate unsteady flow fields and exhibit horizontal translation, rotation, and oscillation. Empirical formulas for drag coefficient, terminal velocity, and ventilation effect are given. Fall trajectory, pressure distribution, wake structure, vapor field, and vorticity field are examined.

Contents

List of Figures

List of Tables

Principal Symbols

Symbol	Unit	Representation
A, A_{proj}	m^2	Area, Projected area
a	μm, —	Radius[*][†], amplitude parameter for SMOSS technique (2.1)
AR	—	Aspect ratio
b	—	Width parameter for SMOSS technique (2.1)
C	$J\ V^{-2}$	Capacitance
c	—	Center size parameter for SMOSS technique (2.1)
C_D	—	Drag coefficient
c_p	$J\ kg^{-1}\ K^{-1}$	Specific heat capacity at constant pressure
C_0	—	Coefficient for surface roughness
D (d)	μm	Maximum dimension (diameter)[*][†]
D_v	$m^2\ s^{-1}$	Diffusivity of water vapor in air[*][†]
$\vec{E}$	$V\ m^{-1}$	Electric field
e_s	Pa	Saturation vapor pressure
$\bar{f}_v$	—	Mean ventilation coefficient
g	$m\ s^{-2}$	Acceleration of gravity[†]
h	μm	Height/thickness[*]
I, I^*	$kg\ m^2$, —	Moment of inertia, Dimensionless moment of inertia
$\mathbf{j_v}$	$kg\ m^{-2}\ s^{-1}$	Vapor flux density

K	W m^{-1} K^{-1}	Thermal conductivity
l, l*	m, —	Length of swing/spiral motion, Dimensionless horizontal displacement
m	kg	Mass
N$_{Sc}$	—	Schmidt number
n	—	Polygonality parameter for SMOSS technique (2.1)
P	Pa	Pressure
R$_d$	J kg^{-1} K^{-1}	Gas constant for dry air
Re	—	Reynolds number
r	—	Radial coordinate
T, T$_c$	K, C	Temperature
u	m s^{-1}	Velocity[†]
V	m^3	Volume
X	—	Best (Davies) number, $\bar{f}_v$ dimensionless quantity (4.14)
α	—	Coefficient in mass-dimension relation (2.20)
β	—	Index in mass-dimension relation (2.20)
γ	—	Coefficient in area-dimension relation (2.21)
δ	m	Boundary layer depth
δ_0	—	Coefficient for boundary layer depth δ
η, η_a	kg m^{-1} s^{-1}	Absolute or dynamic viscosity of fluid, of air
θ	—,rad	Angular coordinate, zenith angle
ν, ν_a	m^2 s^{-1}	Kinematic viscosity of fluid, of air
ρ_a, ρ_s, ρ_v	kg m^{-3}	Densities of air, ice and vapor[†]
Φ	V	Electrostatic potential
σ	—	Index in area-dimension relation (2.21)

[*]International System of Units (SI) when noted

[†]Centimeter-gram-second (cgs) system of units when noted

Chapter 1

Introduction

Consider a tiny, fragile ice crystal falling before you, drifting gently toward the surface of the earth. This is simply one of many beautiful, everyday examples of time-dependent fluid dynamics at low to intermediate Reynolds numbers. When envisioning the fall trajectory of a snow or ice crystal, firsthand experience, or perhaps a bit of imagination, tells us to expect complex translational and rotational motions, such as side-to-side oscillations (fluttering), sideways drifting, and tumbling. The fluttering and tumbling motions of flat bodies falling through a viscous medium has interested scientists for centuries, dating back at least to Newton and Maxwell and is relevant in the study of meteorology and various branches of engineering. The goal of this study is to extend the framework laid out in Cheng et al. (2015) by obtaining the theoretical numerical solutions of the flow fields around four types of planar ice crystals—crystals with sector-like branches, crystals with broad branches, stellar crystals, and ordinary dendrites—of various sizes,

where smaller sizes exhibit steady flow fields and larger sizes demonstrate unsteady flow fields with eddy shedding.

Frozen hydrometeors take on all types of shapes and sizes, from hexagonal ice crystal plates to more complicated dendrites and aggregates. Ice crystals of various shapes and sizes possess varying masses and cross-sectional areas, generating different flow fields, which influence the microphysics of the particles, including their fall velocities, heat dissipation rates, ventilation effects, diffusional growth rates, and collision efficiency with other hydrometeors (Pruppacher and Klett, 1997, Wang, 1982, Wang and Denzer, 1983). Crystal and snow processes influence thunderstorm anvil and other cloud structures, which have important radiative impacts (e.g., Takano and Liou, 1993). Quantitative knowledge of all of these microphysical processes is required for accurate weather and climate predictions, though these processes are not well understood on the scale of individual ice crystals.

Flow fields and fall attitudes can be studied experimentally from field observations of real ice crystals falling through air (e.g., Nakaya and Terada, 1935), tank measurements of model ice crystals falling through viscous liquids (e.g., Jayaweera and Mason, 1965, 1966, List and Schemenauer, 1971, Willmarth et al., 1964), or from theoretical calculations (e.g. Cheng et al., 2015, Hashino et al., 2016, 2014, Ji and Wang, 1991, Wang and Ji, 1997, 2000). More recent studies such as Matrosov et al. (2005) have inferred fall attitudes of ice crystals from radar data and Takahashi (2014) has used a cloud tunnel to investigate growth processes. Observational studies cover a broad range of natural crystal shapes,

though these measurements are subject to large experimental error while tank experiments have small experimental errors ($\approx 10\%$) but only a small sampling of idealized crystal shapes are studied (Heymsfield and Westbrook, 2010). Theoretical calculations are essential for fully understanding the motions of ice crystals and making meaningful assessments of their role in cloud microphysical processes.

Previous studies have found that small ice crystals exhibit steady fall behaviors, though very small particles (Reynolds number $Re \leq 1$) likely fall with random orientations (Wang, 2013). Planar hexagonal ice crystals in the intermediate Reynolds range ($1 \leq Re \lesssim 100$) fall steady with horizontally oriented basal planes (Figure 2.2). The upper Reynolds limit for steady motion for planar ice crystals with narrow branches, such as e.g. stellar crystals and dendrites, is $Re \approx 200$. Note, these Reynolds ranges are not exact, and different crystal habits, such as ice columns, have different Reynolds ranges that describe steady fall behavior. The flow fields become unsteady and downstream eddy shedding begins to occur for increasingly larger ice crystals. Eventually secondary motions occur simultaneously, such as rotational, oscillatory, and weaving translational motions that are easy to envision, though complicated to understand.

The use of numerical methods for studying flow fields around particles is nothing new. For example, Dennis and Chang (1969), Kawaguti (1953), Nieuwstadt and Keller (1973), Thom (1933) studied the two-dimensional flow past circular cylinders, and Masliyah and Epstein (1970), Rimon and Lugt (1969) studied flow around thin, axisymmetric oblate

spheroids. Often, early studies made assumptions and approximations that are not realistic. For example, Schlamp et al. (1975) assumed falling ice crystals could be approximated as infinitely long circular cylinders, reducing the three-dimensional problem to one in two dimensions. Similarly, Pitter et al. (1973) approximated hexagonal ice crystals as thin oblate spheroids.

Ji and Wang (1990, 1991) and Wang and Ji (1997) used realistic columnar and hexagonal plate ice crystal shapes in their flow field calculations, obtaining steady and unsteady flow fields for low to intermediate Reynolds numbers. One limitation of these studies, and all prior studies, is the assumption that the ice crystals fall with their largest dimension (length-axis for columnar crystals; basal plane for hexagonal plates) oriented perpendicular to the direction of fall, which is the expected orientation of steady falling ice crystals (Pruppacher and Klett, 1997). Of course, firsthand experience tells us that snow and ice crystals do not fall down straight with no changes in orientation, rather the motion depends on the Reynolds number and dimensionless moment of inertia (e.g., Field and Klaus, 1997, Willmarth et al., 1964). Unstable fall behavior has been shown to occur for plate-like crystals as small as 1.23 mm, corresponding to $Re = 47$, and that the orientation and horizontal motions are important in crystal aggregation (Kajikawa, 1992).

While studies such as Hashino et al. (2014) provide insight into the flow fields of ice crystals with fixed inclined orientation of the crystal's largest dimension, even these results would differ from the realistic case of unsteady freely falling crystals. Up to this point, by

not simulating freely falling ice crystals, the previous results suggest that, while crystal fall motions generate flow fields, the crystals themselves do not respond to changes in the flow fields. Cheng et al. (2015) addresses this deficiency and provides the first numerical results for the flow field calculation of freely falling hexagonal ice plates, allowing for the hydrodynamic forces of the flow field to influence the plate, such that oscillatory, rotational and translational motions are allowed. In a similar manner, Hashino et al. (2016) simulates the flow fields around freely falling columnar crystals.

In addition to calculating flow fields, previous theoretical studies have also investigated the enhancement of ice crystal diffusional growth due to falling motion, or the ventilation effect (e.g., Cheng et al., 2014, Ji and Wang, 1999, Masliyah and Epstein, 1970, Pitter et al., 1974). Earlier studies approximated hexagonal plates as thin oblate spheroids, though with the advance of computer technology it is possible to perform calculations using the true shapes of ice plates. Similar to Cheng et al. (2014), in this study specific water vapor density boundary conditions are prescribed in order to calculate the ventilation effect, or the enhancement in growth by vapor diffusion due to falling motion.

Working to extend the framework laid out by Cheng et al. (2015) and previous studies, the flow fields of four additional types of planar ice crystals—crystals with sector-like branches, crystals with broad branches, stellar crystals, and ordinary dendrites—are calculating for crystal size ranges of 0.1 to 0.5 mm and 1 to 5 mm in maximum dimension. The methods of this study are split into two chapters; chapter 2 addresses the properties

of the crystals and fluid while chapter 3 presents the math and physics behind the calculation of the fluid flow fields and includes information on the meshing process and the computational fluid dynamics solver. The results are presented in chapter 4. Finally, a discussion of the results and a summary of the work are given in chapter 5.

Chapter 2

Crystal & Fluid Properties

The flow fields described by falling objects depend on the properties of both the object and of the fluid. Six quantities work together to determine the falling motion of objects: the diameter of the object d, its thickness h, the density of the object ρ_s, and of the fluid ρ_a, the kinematic viscosity of the fluid ν and the gravitational acceleration g. From these, three non-dimensional numbers arise: the aspect ratio AR, the dimensionless moment of inertia I^*, and the Reynolds number Re. This chapter is concerned with the dimensional and non-dimensional quantities used to describe crystal fall behavior.

2.1   Ice Crystal Properties

This study focuses on crystals with sector-like branches, crystals with broad branches, stellar crystals and ordinary dendrites. Subsection 2.1.1 presents the categorization of

and general background on planar ice crystals, along with a mathematical method of categorizing crystals. The geometric properties of planar ice crystals are considered in Subsection 2.1.2.

2.1.1 Classification

Ice crystals have been classified into various categories throughout history (e.g., Magono and Lee, 1966, Mason, 1971, Nakaya and Sekido, 1936) and are continuously revised to include new categories for snow crystals, such as those discovered in Polar Regions. Figure 2.1 illustrates the 80 crystal classes according to the classification efforts of Magono and Lee (1966). More recently, Kikuchi et al. (2013) provide detailed information, photographs and schematic summaries of 121 types of snow crystals, ice crystals, and other solid precipitation particles, including needle-type crystals, dendrite-type crystals, column-type aggregate crystals, and lump graupel, to mention a few.

The wide variety of ice crystal shapes, or "habits" are due to crystal growth processes. From a crystallographic viewpoint, crystals generally exhibit a hexagonal, six-sided symmetry, comprised of the c axis normal to the two basal faces, and the a axis, which is parallel to the basal face (Figure 2.2). Crystal habit is determined by preferential growth along these planes and axes and is a complicated function of a variety of factors, including environmental temperature and supersaturation with respect to ice (e.g., Hallett, 1965, Mason, 1953, Ono, 1970, Young, 1993).

Figure 2.3 depicts the four crystal types used for this flow field investigation. They

N1a Elementary needle	C1f Hollow column	P2b Stellar with sectorlike ends	
N1b Bundle of elementary needles	C1g Solid thick plate	P2c Dendrite with plates at ends	
N1c Elementary sheath	C1h Thick plate of skeletal form	P2d Dendrite with sectorlike ends	
N1d Bundle of elementary sheaths	C1i Scroll	P2e Plate with simple extensions	
N1e Long solid column	C2a Combination of bullets	P2f Plate with sector extensions	
N2a Combination of needles	C2b Combination of columns	P2g Plate with dendrite extensions	
N2b Combination of sheaths	P1a Hexagonal plate	P3a Two branches	
N2c Combination of long solid columns	P1b Sector plate	P3b Three branches	
C1a Pyramid	P1c Broad branch	P3c Four branches	
C1b Cup	P1d Stellar	P4a Broad branch with 12 branches	
C1c Solid bullet	P1e Ordinary dendrite	P4b Dendrite with 12 branches	
C1d Hollow bullet	P1f Fernlike dendrite	P5 Malformed crystal	
C1e Solid column	P2a Stellar with plates at ends	P6a Plate with spatial branches	

P6b Plate with spatial dendrites	CP3d Plate with scrolls at ends	R3c Graupel-like with nonrimed extensions	
P6c Stellar with spatial plates	S1 Side planes	R4a Hexagonal graupel	
P6d Stellar with spatial dendrites	S2 Scalelike side planes	R4b Lump graupel	
P7a Radiating assemblage of plates	S3 Side planes with bullets and columns	R4c Conelike graupel	
P7b Radiating assemblage of dendrites	R1a Rimed needle	I1 Ice particle	
CP1a Column with plates	R1b Rimed columnar	I2 Rimed particle	
CP1b Column with dendrites	R1c Rimed plate or sector	I3a Broken branch	
CP1c Multiple capped column	R1d Rimed stellar	I3b Rimed broken branch	
CP2a Bullet with plates	R2a Densely rimed plate or sector	I4 Miscellaneous	
CP2b Bullet with dendrites	R2b Densely rimed stellar	G1 Minute column	
CP3a Stellar with needles	R2c Stellar with rimed spatial branches	G2 Germ of skeletal form	
CP3b Stellar with columns	R3a Graupel-like snow of hexagonal type	G3 Minute hexagonal plate	
CP3c Stellar with scrolls at ends	R3b Graupel-like snow of lump type	G4 Minute stellar	
		G5 Minute assemblage of plates	
		G6 Irregular germ	

FIGURE 2.1: Magono-Lee classification of naturally occurring snow crystals from Magono and Lee (1966). Included by permission of Hokkaido University; reproduced figure courtesy of Pao K. Wang.
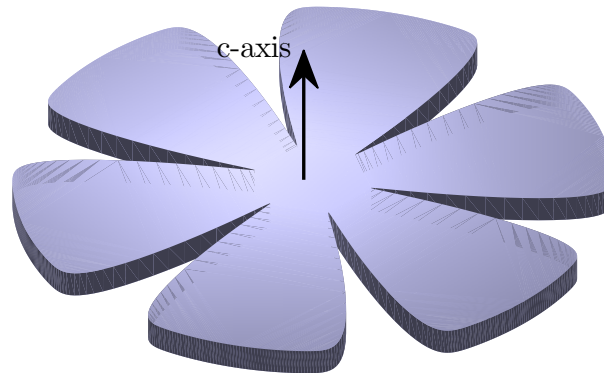

FIGURE 2.2: Schematic representation of the c axis of a sector plate ice crystal. Here, the c axis is normal to the basal plane.

correspond to planar crystals under the Magono and Lee (1966) classification scheme. According to their classification method, crystals with sector-like branches (hereafter, sector plates) are assigned a classification identification tag of *P1b*, where *P* represents planar crystals, *1* refers to the sub-category "regular crystal developed in one plane," and *b* signifies that the sector plate is the second of six crystals with the *P1* classification. In a similar fashion, the other ice crystal types that are studied included the broad-branched crystal *P1c*, stellar crystal *P1d*, and ordinary dendritic crystal *P1e*. This work builds on the investigation into the aerodynamics of hexagonal ice plates *P1a*, by Cheng et al. (2015) and thus were not considered for this study. The sixth planar type, regular crystal—fernlike crystals *P1f*—are not considered due to both their similarity to the ordinary dendritic crystal and a lack of sufficient fall velocity data from Kajikawa (1972) and Mitchell (1996), used in part to predict terminal velocity initial conditions for the flow field calculations.

Having qualitative classification schema are extremely useful for understanding the descriptive categorization of ice and snow crystals, however these classifications are inadequate for performing physical calculations, which require quantitative classification. There are a handful of possible ways to quantitatively classify frozen hydrometeors. For example, Lim et al. (2013) devised a classification methodology of snow particles, such as crystals, aggregates, rimed snow, etc., by utilizing radar reflectivity fields, which can be used for determining more accurate estimates of snowfall rates. Another classification approach, using simple mathematical functions to describe hydrometeor shapes, is a more suitable approach for studying physical properties, such as heat diffusion rates, flow fields
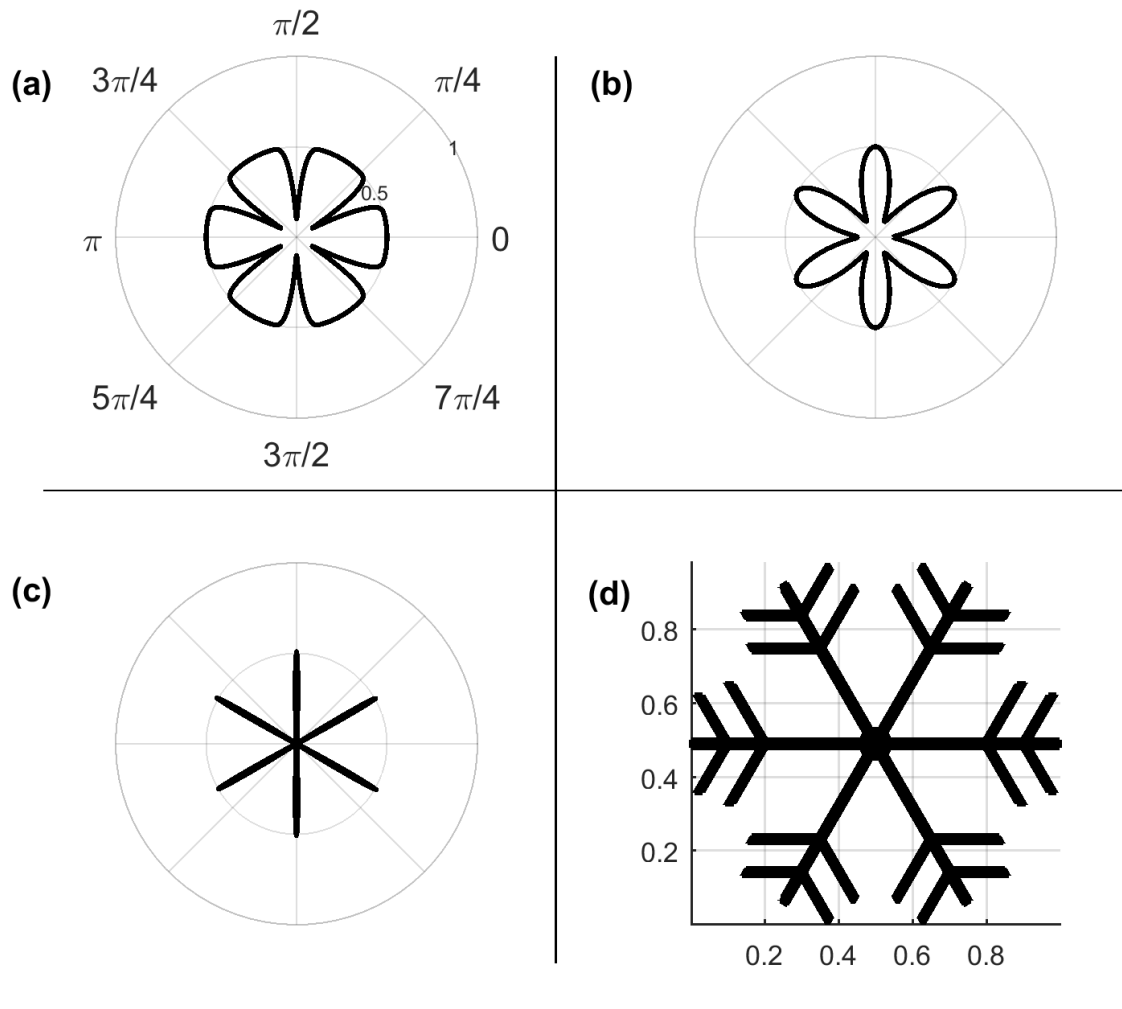
FIGURE 2.3: The 2D crystal shapes considered in this study: (a) sector plates; (b) broad-branched crystal; (c) stellar crystal; and (d) ordinary dendritic crystal.

around hydrometeors, and light scattering properties by ice crystals in cirrus clouds (e.g., Liou, 1992). The mathematical approach of hydrometeor classification is employed in this study and is based on the efforts of numerous previous studies (e.g., Auer and Veal, 1970, Wang, 1982, 1987, 1997, 1999).

Auer and Veal (1970) were among the first to study the dimensions of natural ice crystals and created empirical relationships that describe the dimensions, namely height,

diameter, width, and length, of a wide range of ice crystals. Their results work well for simple-shaped ice crystals, such as hexagonal plates and columnar ice crystals, however their relationships make it difficult to analyze physical and geometrical properties, such as calculating the volume of complex ice crystals. Addressing this topic, a series of papers in the 1980s and 1990s provide simple, mathematical functions to describe the two-dimensional shapes of conical hydrometeors (Wang, 1982), columnar ice crystals (Wang, 1997), polygonally symmetric particles (Wang, 1987), and, the topic of this thesis, planar ice crystals (Wang and Denzer, 1983).

The geometries of three ice crystals investigated in this study are the product of a convenient, simple technique first discussed in Wang and Denzer (1983), and revised into more general forms and for three dimensions in a subsequent publication (Wang, 1997). This technique, termed the Successive Modification of Simple Shapes (SMOSS), can be used to generate a variety of idealized shapes representing observed ice crystals.

SMOSS involves applying a mathematical function to a simple shape in order to generate a more complex shape (Wang, 1997). For example, to create the shape of a planar ice crystal, one can start with an equation describing a circular disk, then use a periodic sine or cosine function to modulate the width, amplitude and polygonality of a complex shape. The general form of the equation used to modify crystal shape in this study, in polar coordinates, is

$$r = a[\sin^2(n\theta)]^b + c, \tag{2.1}$$

TABLE 2.1: The parameters for the three crystal types produced using the SMOSS technique. The Magono and Lee symbols, along with the amplitude parameter (a), width parameter (b), center size parameter (c) and polygonality parameter (n) are presented.

Crystal type	Shape/ID	a	b	c	n
Sector plate	✽ P1b	-0.4	10	0.5	3
Broad-branch	✳ P1c	0.4	1	0.1	3
Stellar	✳ P1d	0.5	100	0.01	3

where r is the radial coordinate and θ is the angular coordinate ($0 \leq \theta \leq 2\pi$). The parameter a modulates the amplitude of the peak (termed the amplitude parameter; $c \leq a \leq \infty$), b adjusts the peak width (width parameter; $0 \leq b \leq \infty$), c represents the size of the center disk (center size parameter; $0 \leq c \leq \infty$), and n dictates the number of peaks, and must be a multiple of $1/2$ in order to satisfy the condition of a self-closing curve (polygonality parameter; n: 0, 0.5, 1, 1.5, 2, $\cdots$). In an attempt to aid the reader in better understanding the modulating role of each parameter, Figure 2.4 presents an application of the SMOSS technique on the square of the sine function, $r = \sin^2(\theta)$, parameter by parameter, and Table 2.1 provides the values of the parameters used to create them.
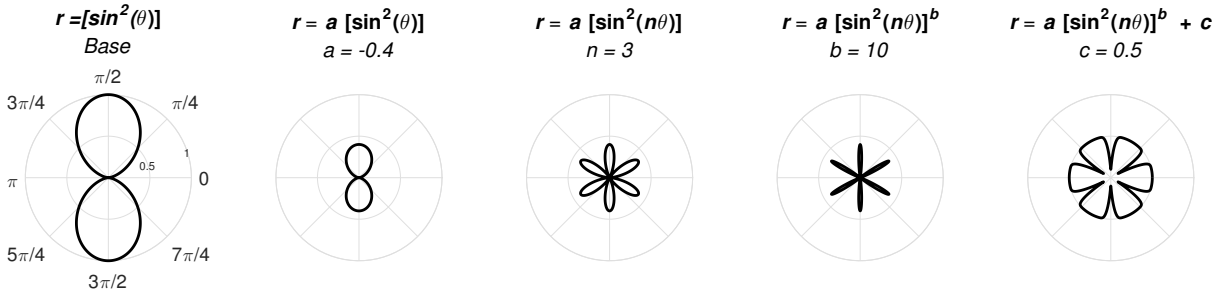

FIGURE 2.4: A demonstration of the application of the SMOSS technique applied to the function $r = \sin^2(\theta)$ over the domain $0 \leq \theta \leq 2\pi$.

In this study, the 2D shapes of three planar crystal types are developed using the SMOSS technique (Figure 2.3, Table 2.1). Two-dimensional SMOSS was chosen over the 3D alternative because the availability of AutoDesk AutoCAD® software allowed for the seamless extrusion of 2D surfaces, resulted in smaller file sizes when exporting the curves to stereolithography (STL) file format for geometry and mesh generation (Subsection 3.2.2), and was already employed for calculating the moments of inertia (Subsection 2.1.2). It is noted that growth processes (nucleation, deposition, collision) are not considered when arriving at the 'perfect' mathematically defined shapes. Keep in mind that observed ice crystals would have imperfections in symmetry compared to the idealized ice crystals produced using the SMOSS method. The geometry of the dendritic crystal is created using AutoCAD software.

2.1.2   Dimensions & Mass

Using empirical relationships to describe ice crystal dimensions for various crystal types began in earnest with the works of Ono (1969) and Auer and Veal (1970). The diameter and thickness of ice crystals affect the crystal's growth, mass, and fall velocity. A few key relationships for crystals used in this work are described below.

By fitting polynomial or power functions to experimental data using a least squares technique, Auer and Veal (1970) present empirical relationships for crystal types according to the Magono and Lee (1966) classifications and temperature regimes. For crystals of interest in this study, the following power law relationships describe the height/thickness h and diameter d, given in μm:

Sector plates: $h = 2.020\,d^{\,0.449}$, (2.2)

Broad-branched and stellar crystals: $h = 2.028\,d^{\,0.431}$, (2.3)

Dendritic crystals: $h = 2.801\,d^{\,0.377}$, (2.4)

and these relationships are shown graphically in Figure 2.5.
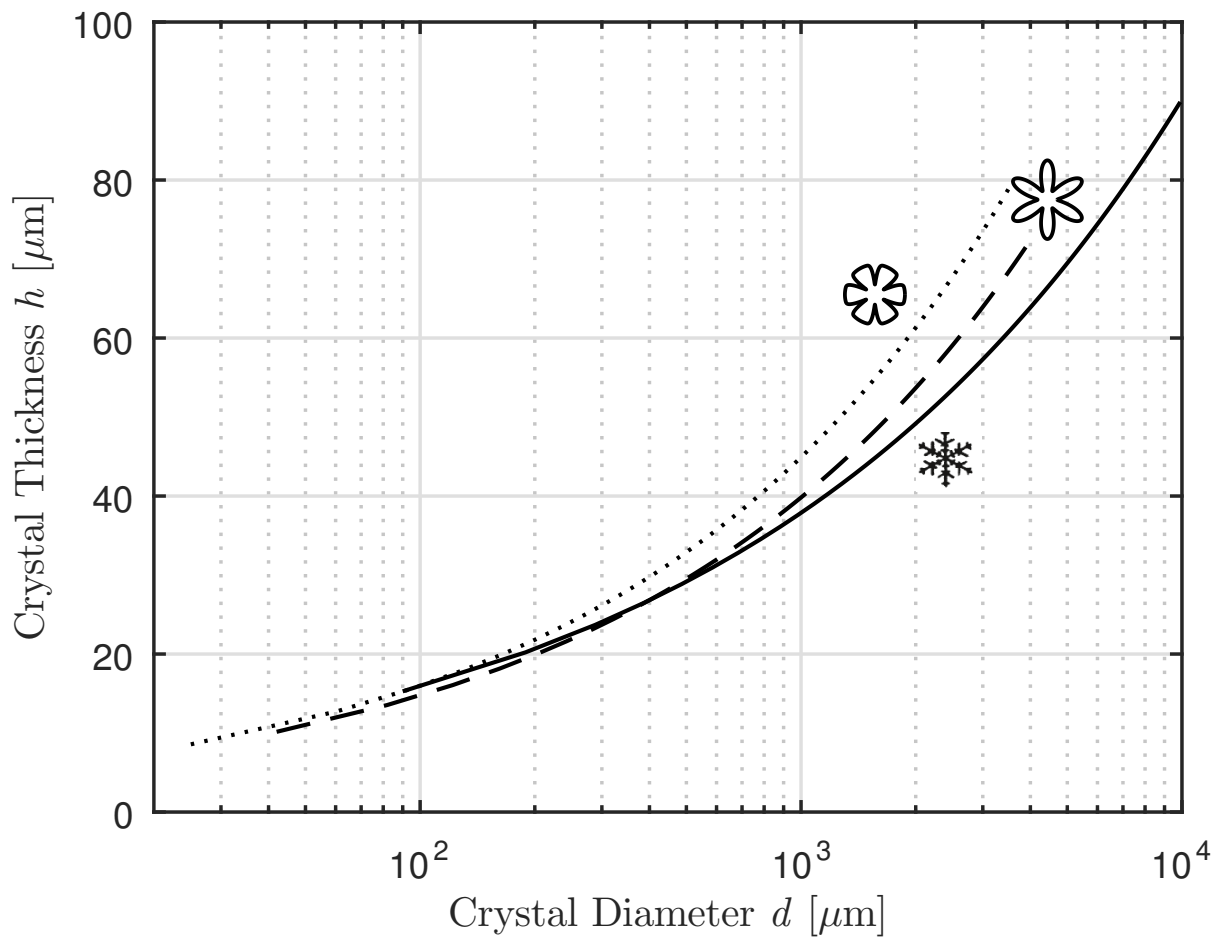

FIGURE 2.5:   Diameter-thickness relationships for: sector plates (dotted), broad-branched/stellar crystals (dashed), and dendritic crystals (solid). The diameter d and thickness h are given in μm. Based on data from Auer and Veal (1970).

The Auer and Veal (1970) diameter-thickness relationships are in general agreement with earlier studies (e.g., Mason, 1953, Ono, 1969, Schaefer, 1947), and subsequent studies (e.g., Hobbs et al., 1974). The Auer and Veal (1970) empirical relationships are the method of choice for this study, since they provide relationships for the variety of the four crystal types of interest.

The diameter and thickness of ice crystals can be conveniently expressed as the non-dimensional aspect ratio AR, or the ratio of an ice crystal's thickness to its diameter (i.e., $AR = \mathrm{h}/\mathrm{d}$). Knowledge of the aspect ratio is especially important for determining radiative properties of ice crystals, such as the asymmetry parameter (e.g., Diedenhoven et al., 2012).

The mass of an object described by a 2D curve for a given thickness is determined by solving for the volume and multiplying by the density of the material. Here, the density of ice, ρ_s, is assumed to be 916.68 kg m^{-3}. The thickness, h, depends on the type of crystal, and is a function of the diameter (Equations (2.2) to (2.4)). The area A enclosed by a curve generated from the SMOSS technique is calculated by integrating the right hand side of Equation 2.1:

$$A = \frac{1}{2} \int_0^{2\pi} r^2 d\theta \tag{2.5}$$

and thus the volume V is: $V = A\ h$. The equation used to determine the mass m is simply: $m = \rho_s V$. Additionally, AutoCAD software provides a tool for calculating the area enclosed by the curve and the volume of an extruded surface, and is utilized in this study.

The motion of ice crystals falling through the atmosphere also depends on the objects'
moments of inertia or the distribution of mass with respect to a chosen axis of rotation,
and a measurement of an objects resistance to rotational acceleration. The most general
form of the moment of inertia, I, is given by

$$I = \int r^2 dm, \tag{2.6}$$

and the dimensionless moment of inertia I^* is defined as

$$I^* = \frac{I_a}{\rho_a D^5} \tag{2.7}$$

where I_a specifies the moment of inertia about the a axis of the ice plate (i.e., parallel to
the basal face, see Figure 2.2), ρ_a is the density of air, and D is the maximum dimension
measured along the a axis (diameter for planar ice crystals). The calculation of I_a was
performed with the AutoCAD software. Willmarth et al. (1964) found the free-fall pattern
of disks generally depends on Re and I^*, while the Best number X and I^* have been shown
to determine the onset of unstable falling motion for plate-like ice crystals (Kajikawa,
1992). The effects of the fluid on falling body motion is expected to be greatest for small
I^*; the crystal moment of inertia dominates for large I^* (Field and Klaus, 1997).

2.2 Fluid Properties

The following subsections present the density, viscosity and thermal conductivity, and diffusivity of air at 900 hPa, -10 C.

2.2.1 Air Density & Viscosity

The density of moist air is a function of pressure, temperature and humidity. The following equation describe the calculation of the density of air ρ_a, based on Yau and Rogers (1996) and Brutsaert (1982):

$$\rho_a = \frac{P}{R_d\ T}\ \left(1 - \frac{0.378\ e_s}{P}\right), \tag{2.8}$$

where P is the atmospheric pressure (in Pa), R_d is the gas constant for dry air (287.05 J kg^{-1} K^{-1}), T is the temperature (in K), and e_s is the saturation vapor pressure (in Pa). The equation for e_s, with temperature in degrees Celsius T_C:

$$e_s = 611.2\ \exp\left(\frac{17.67\ T_c}{T_c\ +\ 243.5}\right), \tag{2.9}$$

is the result of an empirical fit to data, since solving the Clausius-Clapeyron equation for the saturation pressure of water vapor pressure involves a difficult calculation due to the temperature dependence of latent heat (Pruppacher and Klett, 1997). For the atmospheric conditions in this study—atmospheric pressure and temperature of $P = 900$ hPa and $T = $ -10 C, respectively—-the density of air is $\rho_a= 1.19$ kg m^{-3}.

Another relevant property of the fluid is the viscosity. Viscosity is a measurement of a fluid's resistance to flow. The absolute and kinematic viscosity are calculated, respectively, using the following:

$$\eta = 1.72e - 5 \ \left(\frac{393}{T \ + \ 120}\right) \left(\frac{T}{273.15}\right)^{1.5} \tag{2.10}$$

$$\nu = \frac{\eta}{\rho_a} \tag{2.11}$$

where η is the absolute viscosity (kg m^{-1} s^{-1}; also known as the dynamic viscosity), and ν is the kinematic viscosity [m^2 s^{-1}](Yau and Rogers, 1996). A dimensionless quantity is formed by combining the fluid viscosity with a characteristic velocity, which we define using the terminal velocity u_∞, and the diameter of an object:

$$Re = \frac{u_\infty \ d\rho_a}{\eta_a} = \frac{u_\infty \ d}{\nu_a}, \tag{2.12}$$

where Re is the Reynolds number. The Reynolds number provides a dimensionless measurement of the flow speed; low Re tend to correspond to laminar, viscous flow in which the viscous forces dominate, whereas turbulent flow is generally characterized by high Re, where the flow is dominated by its inertial forces.

2.2.2 Thermal Conductivity & Diffusivity

The thermal conductivity, diffusivity and specific heat capacity are fluid properties that describe the fluid's ability to store and transfer heat and are critical for modeling processes that deal with heat. The thermal conductivity describes how a material conducts heat,

and while there are a number of ways to measure it, a simple equation for calculating the thermal conductivity, accurate to within 1% over the temperature range -30 to 230°C, is used:

$$K = 0.0264 \left(\frac{T}{300}\right)^{0.8646} \tag{2.13}$$

where K is the thermal conductivity of the air (W m^{-1} K^{-1}) (Dixon, 2007). Intimately related to the thermal conductivity is the diffusivity, or the measure of the rate of heat transfer of a material from the "hot" side to the "cold" side. The diffusivity of water vapor in air D_v is the ratio of the thermal conductivity K to the product of the density ρ and specific heat capacity at constant pressure c_p (i.e., $D_v = {}^K/\rho c_p$). It can also be given by the empirical relation from Hall and Pruppacher (1976):

$$D_v = 0.211 \left(\frac{T}{T_0}\right)^{1.94} \left(\frac{P_0}{P}\right), \tag{2.14}$$

where $T_0 = 273.15$ K and $P_0 = 1013.25$ hPa, and D_v is given in cgs units cm^2 s^{-1}. This relation is valid for the temperature range -40 to 40 C.

2.3   Terminal Velocity

The terminal velocity u_∞ of falling ice crystals and snowflakes has been a topic of interest and debate since the Nakaya and Terada (1935) paper, where the velocity of individual crystals were measured through crystal position observations with the naked eye and the time was measured with a stop watch. Subsequent studies measured fall velocity using photographic techniques with stroboscopic illumination (e.g., Higuchi, 1956, Langleben,

1954, Schaefer, 1947, Zikmunda and Vali, 1972), and radar (e.g., Marshall, 1953). The need for accurate predictions of terminal velocity is critical for modeling cloud processes, which have been shown to be sensitive to the parameterization of fall velocities (Starr and Cox, 1985). For the purposes of this study, an accurate terminal fall velocity is required to avoid large displacements of the ice crystal in the $\hat{z}$ direction, which would require a larger domain size to ensure proper boundary conditions.

Subsection 2.3.1 describes the process of using dimensionless quantities, the Reynolds Re and Best X numbers, to predict the terminal fall velocity given a relationship between Re and X, which is determined in laboratory or field experiments (e.g., Knight and Heymsfield, 1983). Subsection 2.3.2 presents the technique used to predict the initial guess terminal fall velocities of the ice crystal flow field simulations.

2.3.1 Theoretical Relationship between Re & X

A theoretical approach to determining ice crystal terminal velocities involves deriving relationships between crystal dimensions, fluid properties and fall velocities from aerodynamic principles, based on the conclusion that when a planar ice crystal falls, with its basal face perpendicular to the direction of fall, the terminal velocity is reached when the object's weight is balanced by the air drag. For example

$$u_\infty = \sqrt{\frac{2mg}{\rho_a A_{proj} C_D}}, \tag{2.15}$$

where A_{proj} is the object's projected area (in the direction normal to the flow) and C_D is the drag coefficient (Magono, 1954). The issue with Equation 2.15 is the dependence on the drag coefficient C_D, which varies with Reynolds number and is therefore dependent on u_∞.

Ice crystal terminal velocities are typically calculated by finding a relationship between the Reynolds number and the *Best*, or *Davies* number X

$$\text{X} = C_D\text{Re}^2 = \frac{2mg\rho_a D^2}{A_{proj}\eta^2}, \qquad (2.16)$$

where D is the object's maximum dimension (diameter d for planar ice crystals)(List and Schemenauer, 1971). Note that X has no dependence on u_∞, and depends only on the properties of the object and fluid.

In early studies, the Best number for ice crystals was based on more simple geometries. For example, the fall velocity of plate-like crystals can be estimated from drag data by approximating their shape as thin, oblate spheroids (Jayaweera and Cottis, 1969, Pitter et al., 1973). Once Re, X, and a relationship between the two is known, the terminal velocity can be calculated from the Reynolds number, since Re = $^{\text{U}_\infty}\text{D}/\nu$. The Re-X relationships were algebraic and often contained velocity adjustment coefficients dependent on the ice crystal aspect ratio (e.g., Beard, 1980, Jayaweera and Cottis, 1969, Pruppacher and Klett, 1997). This approach was followed by (e.g., Cornford, 1965, Heymsfield, 1972, Jayaweera, 1972, Jayaweera and Ryan, 1972, Kajikawa, 1971, 1972, 1973, Michaeli, 1977),

and the results were often limited to specific flow regimes (i.e., Re $\lesssim$ 100) and crystal orientation (i.e., the broadest dimension of a thin disk normal to the direction of fall) (Pruppacher and Klett, 1997).

2.3.2 Power Law Relationship

Having analytically continuous fall speed-dimensional power law expressions are a desirable alternative to various relationships for differing Re, and the approach has been widely used for fall velocity expressions in publications such as Heymsfield et al. (2007a), Heymsfield and Kajikawa (1987), Heymsfield et al. (2007b), Jiusto and Bosworth (1971), Khvorostyanov and Curry (2002, 2005), Langleben (1954), Locatelli and Hobbs (1974), Mitchell (1996). Additionally, using projected area- and mass-dimensional power laws instead of oblate spheroid geometry approximations results in calculation improvements (Mitchell, 1996). This type of approach is used to model cloud processes, such as the evolution of cirrus clouds, because it is simple and accurate (Liu et al., 2003).

Mitchell and Heymsfield (2005) provide a velocity power law for the calculation of the terminal velocities of many ice particles using a continuous Re-X relationship over a wide range of Re and X, in cgs units:

$$u_\infty = A_v D^{B_v}. \tag{2.17}$$

Here, the velocity power law coefficients and power index are

TABLE 2.2: Coefficients of mass- and area-power laws for ice crystals used in the calculations of a_{Re}, b_{Re} and X from Mitchell (1996).

	Mass		Area	
Crystal type	α	β	γ	σ
Sector plates (P1b)				
40 μm $\leq$ D $\leq$ 2000 μm	0.00142	2.02	0.55	1.97
Broad-branched crystal (P1c)				
100 μm $\leq$ D $\leq$ 1000 μm	0.000516	1.80	0.21	1.76
Stellar crystal (P1d)				
Plane dendrites(P1e)				
90 μm $\leq$ D $\leq$ 1500 μm	0.000270	1.67	0.11	1.63

$$A_v = a_{Re}\nu^{(1-2b_{Re})}\left(\frac{2\alpha g}{\rho_a\gamma}\right)^{b_{Re}}, \text{ and} \tag{2.18}$$

$$B_v = b_{Re}\left(\beta - \sigma + 2\right) - 1, \tag{2.19}$$

where α, β, γ, and σ are coefficients and indices from the mass- and area-dimensional power law expressions for ice crystals, respectively:

$$m = \alpha D^{\beta}, \quad \text{and} \tag{2.20}$$

$$A = \gamma D^{\sigma}, \tag{2.21}$$

which vary with crystal habit and size, and are given in Table 2.2. Note, Mitchell (1996) assumed stellar crystals to be representative of plane dendrites. Under this same assumption, the mass and area parameters for stellar crystals are also used for dendritic crystals for establishing a first approximation of terminal velocities in this study.

The dimensionless Reynolds and Best number can now be expressed in terms of (2.20) and (2.21) as:

$$X = \frac{2\alpha g \rho_a D^{\beta+2-\sigma}}{\gamma \eta^2}, \tag{2.22}$$

The drag terms that relate Re and X, a_{Re} and b_{Re}, are:

$$a_{Re} = \frac{C_2 \left[(1 + C_1 X^{1/2})^{1/2} - 1 \right]^2}{X^{b_{Re}}}, \tag{2.23}$$

$$b_{Re} = \frac{C_1 X^{1/2}}{2 \left[(1 + C_1 X^{1/2})^{1/2} - 1 \right] (1 + C_1 X^{1/2})^{1/2}}, \tag{2.24}$$

where $C_1 = {}^4/\delta_0^2 C_0^{1/2}$ and $C_2 = {}^{\delta_0^2}/4$. The constants δ_0 and C_0 are the boundary layer depth and drag coefficients from boundary layer theory derived for ice particles, having values of 5.83 and 0.6, respectively, determined by Böhm (1989) and used by Mitchell and Heymsfield (2005). It is noted that the terminal velocity prediction was generally an underestimation, so much so that for larger ice crystals (i.e., $d \geq 1$ mm) the surface roughness parameters from Abraham (1970), $\delta_0 = 9.06$ and $C_0 = 0.292$, were used in this study. The theoretical terminal velocities from the simulations could possibly be explained by deviations in natural ice crystal geometries from the highly idealized crystals simulated in this study. For instance, an idealized broad-branched crystal with an equivalent maximum dimension (diameter), thickness, and ice density as a natural crystal will likely serve as the upper bound for the mass of this type of crystal, since natural

crystals exhibit non-uniform growth, thus a smaller basal face surface area. This suggests the terminal velocity of an idealized crystal is the upper bound for that of a natural ice crystal. With differences in natural and idealized geometries in mind, more precise terminal velocities used to initialize the ice crystal flow simulations were attained by a trial and error method, using Equations (2.17) to (2.24) to provide a reasonable first guess.

2.4   Ventilation Coefficient

Diffusion growth is one of two general processes of hydrometeor growth, the other being growth through collision and coalescence with other hydrometeors. Diffusion growth occurs when an ice crystal is in an environment that is supersaturated (with respect to the crystal), resulting in a water vapor flux towards the surface of the crystal, causing an increase in mass. For a stationary crystal suspended in a supersaturated environment, the vapor density distribution should be highly symmetric, depending only on the radial coordinate r. Of course, in reality, hydrometeors fall relative to air, and this motion results in an asymmetric vapor density field, responding to the resultant flow field. The vapor density gradient will generally be enhanced upstream of the particle, and relaxed in the wake, compared to the symmetry stationary case (Figure 2.6). When integrated over the entire surface of the ice crystal, the magnitude of the vapor flux will always be greater than the surface integrated vapor flux of a stationary crystal. This enhancement of the vapor flux implies an enhancement of the diffusion growth rate, and is known as the *ventilation effect*. The enhancement factor due to motion, the *ventilation coefficient*, is determined by comparing the diffusion growth rate of a falling ice crystal to that of a

stationary crystal. Conversely, for an ice crystal in a subsaturated environment given the same temperature, pressure, and Reynolds number, motion induces an enhancement in the evaporation rate relative to a stationary crystal by the same factor, the ventilation coefficient.
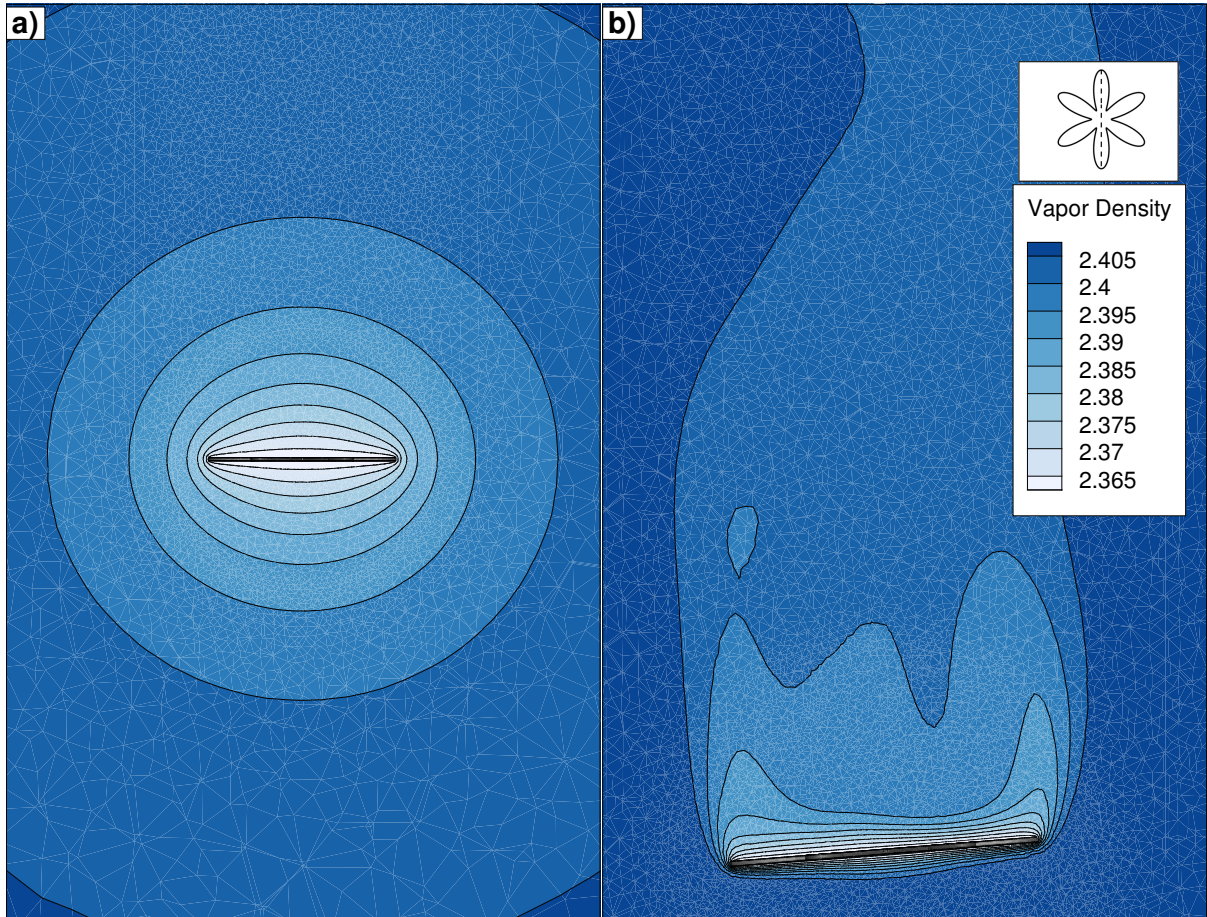

FIGURE 2.6: Example vapor density distributions for: (a) a stationary broad-branched crystal; (b) a broad-branched crystal falling through air. The cross-section location is indicated by the dashed line in the upper righthand corner of the figure and applies to both frames.

Subsection 2.4.1 provides the physical framework for determining the ventilation coefficient of an idealized, spherical water drop and Subsection 2.4.2 presents the adjustments

required to arrive at the same conclusion by numerically solving for diffusion growth for complicated ice crystal geometries.

2.4.1   Theoretical Calculation

For simplicity, consider a spherical water drop of radius a falling at a velocity described by the vector $\mathbf{u}$ in air with a water vapor density ρ_v, which is a function of space and time. The flux density vector of water vapor $\mathbf{j_v}$ towards the drop surface is:

$$\mathbf{j_v} = -D_v \nabla \rho_v + \rho_v \mathbf{u}, \tag{2.25}$$

where $-D_v \nabla \rho_v$ is the diffusion flux density component, with D_v being the diffusivity of water vapor in air (Subsection 2.2.2) and $\rho_v \mathbf{u}$ is the convective flux due to the falling motion.

The conservation of mass dictates that ρ_v must also satisfy the continuity equation, such that

$$\frac{\partial \rho_v}{\partial t} = -\nabla \cdot \mathbf{j_v}. \tag{2.26}$$

Substituting (2.25) into (2.26), assuming D_v is constant, and recognizing that $\nabla \cdot \mathbf{u} = 0$ for incompressible flow, we arrive at the unsteady convective diffusion equation for water

vapor:

$$\frac{\partial \rho_v}{\partial t} = D_v \nabla^2 \rho_v - \mathbf{u} \cdot \nabla \rho_v. \tag{2.27}$$

Assuming ρ_v is in steady state (i.e., ρ_v responds immediately to environmental adjustments), the drop diffusion growth rate is given by integrating the vapor flux density over the drop surface:

$$\frac{dm}{dt} = -\oint_s (D_v \nabla \rho_v)_{r=a} \cdot d\mathbf{S}, \tag{2.28}$$

where the integration is carried out over the surface of the water drop S, which is directed in the positive, "outward" radial direction (Ji and Wang, 1999). Regarding the sign convention, the minus sign indicates that the calculation is for the "inward" flux, such that when $\rho_{v,\infty} > \rho_{v,a}$, the growth rate dm/dt is defined as positive.

The mean ventilation coefficient $\bar{f}_v$ is given by

$$\bar{f}_v = \frac{(dm/dt)}{(dm/dt)_0}, \tag{2.29}$$

where $(dm/dt)_0$ is the diffusion growth rate for the stationary drop and $\bar{f}_v$ is the factor by which the vapor flux toward the drop is enhanced as a result of motion.

To solve this numerically, the following boundary conditions for the vapor density distribution are imposed:

$$\rho_v = 2.3613{\times}10^{-3}\,\text{kg m}^{-3} \qquad \text{at} \qquad r = a$$

$$\rho_v = 2.4086{\times}10^{-3}\,\text{kg m}^{-3} \qquad \text{at} \qquad r \to \infty,$$

(2.30)

such that the environment is saturated at the surface of the drop (i.e., 100% relative humidity), and the environment is 2% supersaturated sufficiently far from the drop (i.e., 102% relative humidity). Note, for extremely small drops (i.e., $a \le$ *10 μm*), a correction for the diffusivity of air is required due to the behavior of water vapor as individual molecules, rather than a continuum (Wang, 2013). Also, Equation 2.28 does not address the inherent release or consumption of latent heat associated with the condensation and evaporation phase changes of water substance, which influences the vapor density field. This is discussed in the following section.

2.4.2 Heat Conduction Analogy

In principle, one can determine the theoretical growth rate of ice crystals using the framework laid out in Subsection 2.4.1. Numerically solving for the diffusion growth rate requires a finite computational domain, which requires reconsideration of the boundary conditions (2.30). The inner boundary condition for a spherical drop, where saturation occurs at the surface (i.e., *r=a*), becomes more complicated when considering the complex geometries of ice crystals. Mathematical expressions that describe three-dimensional surfaces, such as those presented in Wang (1999), can remedy this problem by applying

the surface boundary condition at points defined by the radial coordinate. However, since the crystal geometries in this study were chosen to be defined by two-dimensional expressions, this approach is not pursued. For the outer boundary condition, the constraint of a finite domain requires the placement of the domain boundaries sufficiently far away from the crystal, since $r \rightarrow \infty$ cannot be achieved (Ji and Wang, 1999). Additionally, for unsteady flow, a pre-defined constant vapor density at the boundary downstream of the ice crystal is unrealistic. Instead, this condition must be modified such that the vapor field at the downstream boundary is continuous (i.e., $\partial \rho_v / \partial z = 0$).

Fortunately, there exists an alternative method for determining the vapor density distribution without solving the unsteady convective diffusion equation for water vapor (2.27) subject to the boundary conditions (2.30), adjusted for ice crystal geometries and the constraints of a finite computational domain. The *electrostatic analogy* is a method that takes advantage of the versatility of the Euler form of the continuity equation (2.26). Wang (2013) describes how the electrostatic potential Φ of a perfect conductor, along with the induced electric field $\vec{E}$, can be used as an analog to ρ_v for ice crystals with measured or theoretically calculated capacitance C. Accurate capacitance values are not available for the ice crystals studied here. Instead, in a similar manner, the *heat conduction analogy* is used to calculate the diffusion growth rate.

Where water vapor diffusion is a mass transfer process, heat transfer due to motion is a heat diffusion process. The ventilation of heat is analogous to the ventilation of vapor, and the equations and boundary conditions are the same, except temperature replaces vapor

density and the thermal conductivity of air is used in place of the vapor diffusivity. In other words, the transport of temperature is modulated by the same equation governing the transport of water vapor. Thus, Equation 2.25 can be re-written as the vapor flux vector for heat transport $\mathbf{j_h}$ given by Fourier's law: $\mathbf{j_h} = -K_a \nabla T$, where K_a is the thermal conductivity coefficient of moist air through which heat is transported (Pruppacher and Klett, 1997).

Analogous to Equations (2.28) to (2.29), ignoring heat changes due to radiation and frictional dissipation, and again assuming steady-state conditions, the rate of conductive heat transport dq/dt and the ventilation coefficient for heat diffusion become, respectively:

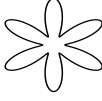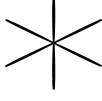$$\frac{dq}{dt} = -\oint_s (K_a \nabla T)_{r=a} \cdot d\mathbf{S}, \tag{2.31}$$

$$\bar{f}_h = \frac{(dq/dt)}{(dq/dt)_0}. \tag{2.32}$$

In the context of cloud physics, the ventilation coefficient for heat diffusion and vapor diffusion are assumed to be equivalent (Pruppacher and Klett, 1997), therefore the ventilation coefficient calculation is determined using the heat conduction method in this study. The mean ventilation coefficient for vapor diffusion is computed directly by numerically solving the heat transport equation for a crystal under moving and stationary conditions (i.e., dq/dt and dq/dt_0, respectively). In order to make temperature analogous to water vapor, great care is taken in prescribing the correct parameters for the energy solver in the fluid dynamics package used, ANSYS® Fluent, Releases 15.0 and 16.2.

2.5   Summary of Properties

Table 2.3 lists the diameters (the largest possible dimension, measured from two opposing tips), aspect ratios, dimensionless moments of inertia, Reynolds numbers, terminal velocities and ventilation coefficients of the four ice crystals investigated: sector plates (P1b under the Magono-Lee classification scheme), crystals with broad branches (P1c), stellar crystals (P1d) and ordinary dendritic crystals (P1e). Here, the aspect ratio, dimensionless moment of inertia, Reynolds number, terminal velocities, and ventilation coefficients are previously described in chapter 2.

TABLE 2.3: Dimensions, dimensionless moments of inertia, Reynolds numbers, terminal velocities and ventilation coefficients for the planar ice crystals investigated in this study.

Type	Diameter d (mm)	Aspect ratio AR	Dimensionless moment of inertia I^*	Reynolds number Re	Terminal velocity u_∞ (cm s^{-1})	Ventilation coefficient fv
P1b	0.2	0.109	3.117	2	14.50	1.15
	0.3	0.087	2.478	5	22.28	1.28
	0.4	0.074	2.108	8	29.08	1.42
	0.5	0.066	1.861	12	34.21	1.54
	1	0.045	1.266	39	54.96	2.10
	2	0.031	0.863	115	80.52	3.39
	3	0.025	0.690	198	92.39	4.30
	4	0.021	0.589	288	100.85	5.09
	5	0.019	0.520	384	107.69	5.94
P1c	0.2	0.099	1.334	1	10.12	1.08
	0.3	0.079	1.052	4	16.14	1.18
	0.4	0.067	0.890	6	20.94	1.30
	0.5	0.059	0.782	9	26.20	1.37
	1	0.040	0.525	31	43.56	1.81
	2	0.027	0.354	93	65.14	2.72
	3	0.021	0.281	175	81.76	3.57
	4	0.018	0.238	258	90.56	4.19
	5	0.016	0.210	345	96.78	4.76
P1d	0.2	0.099	0.110	0.2	1.19	1.01
	0.3	0.079	0.087	0.5	2.09	1.02
	0.4	0.067	0.073	1	3.17	1.05
	0.5	0.059	0.065	2	4.25	1.09
	1	0.040	0.043	7	9.44	1.29
	2	0.027	0.029	25	17.59	1.90
	3	0.021	0.023	53	24.74	2.55
	4	0.018	0.020	89	31.18	3.04
	5	0.016	0.017	133	37.17	3.47
P1e	0.2	0.103	0.690	0.5	3.82	1.03
	0.3	0.080	0.533	1	6.19	1.10
	0.4	0.067	0.444	2	8.59	1.16
	0.5	0.058	0.386	4	10.85	1.23
	1	0.038	0.250	14	19.46	1.61
	2	0.025	0.162	43	29.82	2.75
	3	0.019	0.126	77	35.75	3.77
	4	0.016	0.105	123	43.11	4.93
	5	0.014	0.092	173	48.56	5.87

Chapter 3

Math & Physics of the Flow Field Calculations

This chapter is reserved for a discussion of the theory and numerical methods used to solve the set of differential equations for fluid motion. Technical details about the software used to carry out the flow field calculations are included, along with a discussion of the meshing technique employed.

3.1   Governing Equations

The time-dependent Navier-Stokes equation, coupled with the incompressible flow condition are the governing set of equations for the flow field around falling ice crystals

(Pruppacher and Klett, 1997):

$$\frac{\partial \mathbf{u}}{\partial t} + (\mathbf{u} \cdot \boldsymbol{\nabla}) \mathbf{u} = -\frac{\boldsymbol{\nabla} p}{\rho_a} + \nu \nabla^2 \mathbf{u} + \mathbf{g} \tag{3.1}$$

$$\boldsymbol{\nabla} \cdot \mathbf{u} = 0, \tag{3.2}$$

where $\mathbf{u}$ is the air velocity, p is the static pressure, ν is the kinematic viscosity (Subsection 2.2.1) and $\mathbf{g}$ is the gravitational acceleration, a constant $[0,-9.81]$ m s^{-2}. The boundary conditions are

$$
\begin{aligned}
\mathbf{u} &= 0 & &\text{at } r = a, \\
\mathbf{u} &= u_0 \cdot \hat{\boldsymbol{e}}_{\boldsymbol{z}} & &\text{at } r \to \infty, \\
p &= 0 & &\text{at } r \to \infty
\end{aligned}
\tag{3.3}
$$

where u_0 is the reference wind speed (close to the terminal fall velocity of the ice crystal, see Subsection 2.3), and $\hat{e}_z$ is the unit vector along the fall direction ($\hat{z}$). The first condition is the *no-slip condition*, stating that the fluid will have zero velocity at the rigid ice crystal surface. The second condition states that the velocity of the flow sufficiently far away is not influenced by the presence of the ice crystal and that it is constant. These are the common boundary conditions for these types of problems (Wang, 2013). The unsteady Navier-Stokes equation is necessary because the resulting flow around falling ice crystals at terminal velocity is intrinsically unsteady, exhibiting asymmetries in the flow.

While (3.1) and (3.2) provide the flow field around the ice crystals, they do not provide insight into how the crystal will respond to changes in the flow field. The motion of ice crystals subjected to changing flow fields is determined by solving the *degrees of freedom* (DOF) motion problem for a rigid body in space. For an unrestrained rigid body in space, such as an ice crystal falling through the atmosphere, there are six degrees of freedom (6DOF): three translational motions along x, y and z axes and three rotary motions about the x, y, and z axes (for example, role, pitch, and yaw for airplanes, respectively).

The 6DOF motion is governed by the following equations:

$$\dot{\vec{v_G}} = \frac{1}{m} \sum \vec{f_G} \tag{3.4}$$

$$\dot{\vec{\omega_B}} = L^{-1} \left(\sum \vec{M_B} - \vec{\omega_B} \times L\vec{\omega_B} \right) \tag{3.5}$$

where Equation 3.4 is Newton's second law for the translational motion of the center of gravity and Equation 3.5 is Euler's equation of motion for the rotational motion. Here, $\dot{\vec{v_G}}$ is the translational motion of the center of gravity, m is the mass, $\vec{f_G}$ is the force vector due to gravity, $\dot{\vec{\omega_B}}$ is the angular motion of the object, L is the inertia tensor, $\vec{M_B}$ is the moment vector of the body and $\vec{\omega_B}$ is the rigid body angular velocity vector. The ANSYS, Inc 6DOF solver is employed, which calculates the forces and moments exerted on the planar ice crystal by the ambient flow, and subsequently determines the 6DOF motions of the crystal, including translations and rotations about three perpendicular axes (ANSYS, 2013). These angular and translational motions are then used to update

the position of the rigid body within the dynamic mesh calculation (see Subsection 3.2.2).

3.2   CFD Model

The numerical approach for resolving the flow fields around falling planar ice crystals in this study makes use of Computation Fluid Dynamics (CFD) simulations. The *ANSYS Fluent* CFD model is used to solve the governing differential equations of fluid motion laid out in the previous section. This section works to describe the approach of modeling ice crystal free fall in terms of the solver, *ANSYS Fluent* and the gridding, or mesh, choice.

3.2.1   ANSYS Fluent

The computational fluid dynamics package Fluent 15.0.0 and 16.2.0 of ANSYS, Inc are used for simulating the flow fields around falling planar ice crystals. The CFD solver solves both the Navier-Stokes equation and the 6DOF motion problem at each time step. Instead of simulating crystals falling at their terminal velocity, we treat the equivalent problem of air passing the crystal at the crystal's terminal velocity. This approach improves calculation efficiency by reducing the size of the computational domain through shortening the distance the crystal must fall to reach quasi-steady state (falling at the terminal velocity). However, note the motion and position of the crystal is allowed to change according to the forces imparted on the crystal from the flow field, such that the velocity of the ice crystal will vary depending on the orientation, which acts to modulate the drag force.

For each case, a steady and transient simulation are performed. The steady solution is achieved before allowing the solver to advance in time, serving as an initialization for the transient solution, which reduces computation time and results in a more accurate solution. The following paragraphs provide the solution methods and schemes used within Fluent for the transient calculations.

A coupled pressure-based solver is used, which involves simultaneously solving for the momentum equations and the pressure-based continuity equation in a closely coupled manner. The governing equations are nonlinear and coupled, so the solution process is an iterative one in which the entire set of equations is solved repeatedly until the solution reaches a convergence criterion before stepping forward in time. Figure 3.1 shows the process of the solver.

The Pressure-Implicit with Splitting Operators (PISO) algorithm is chosen for solving the pressure-velocity coupling (Issa, 1986). The scheme satisfies the momentum balance after corrections in pressure are finished, and mass flux is corrected through coupling with neighboring cells. The PISO scheme is used when there are large gradients in velocity.

Gradients, or the value of scalar quantities at cell faces, are computed using the default Least Squares Cell-Based method, which assumes linearity of the solution, is computationally less expensive than other methods but provides a comparable level of accuracy compared to superior methods, such as node-based gradients. For cases with skewed and distorted meshes, such as those used in this study, this method is superior.
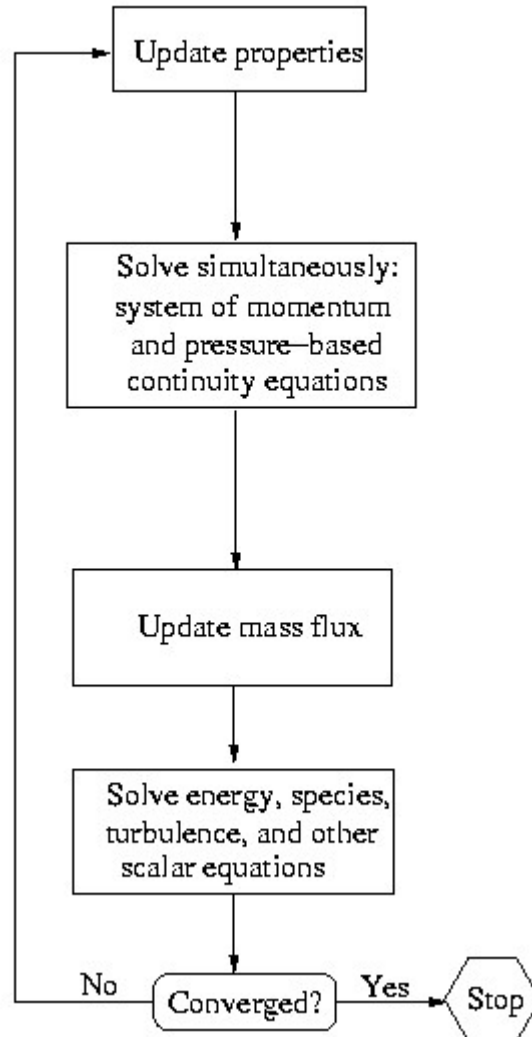
Pressure–Based Coupled Algorithm

FIGURE 3.1: Flow chart for the Fluent pressure solver algorithm. From the ANSYS Fluent Theory Guide.

The Body Force Weighted pressure interpolation scheme is chosen for interpolating pressure values since the body forces are known a priori in the momentum equations. The spatial discretization of the advection of momentum is solved with the Quadratic Upstream Interpolation for Convective Kinematics (QUICK) scheme (Freitas et al., 1985). A Second-Order Upwind Scheme is chosen for the energy discretization, which is used for the calculation of vapor diffusion, and provides high-order accuracy over other methods. The first order option would have difficulty for cases such as these with tetrahedral grids, since the flow is rarely in line with the grid, unlike structured grids. A first order implicit scheme was chosen for the transient formulation with a time step typically set to 1×10^{-4} s, though some simulations required smaller time steps in order to better resolve large displacements due to the forces exerted on the crystal from the flow. Gradients are needed determining values of scalars at cell faces and for computing secondary diffusion terms and velocity derivatives.

Finally, as described, the position and orientation of the crystal changes with time, so a fixed, gridded mesh is unsuitable. ANSYS Fluent provides dynamic mesh capabilities, which allows the mesh to adapt and match the position and orientation of the crystal at each time step. Figure 3.2 shows an example demonstration of the dynamic mesh technique. For each time step, the 6DOF solver determines the position and orientation of the crystal. Next, the mesh is modified in accordance with the crystal's altered position and orientation. In order to maintain mesh quality, diffusion smoothing and re-meshing options are used when the mesh is updated to reflect the 6DOF motions of the crystal.
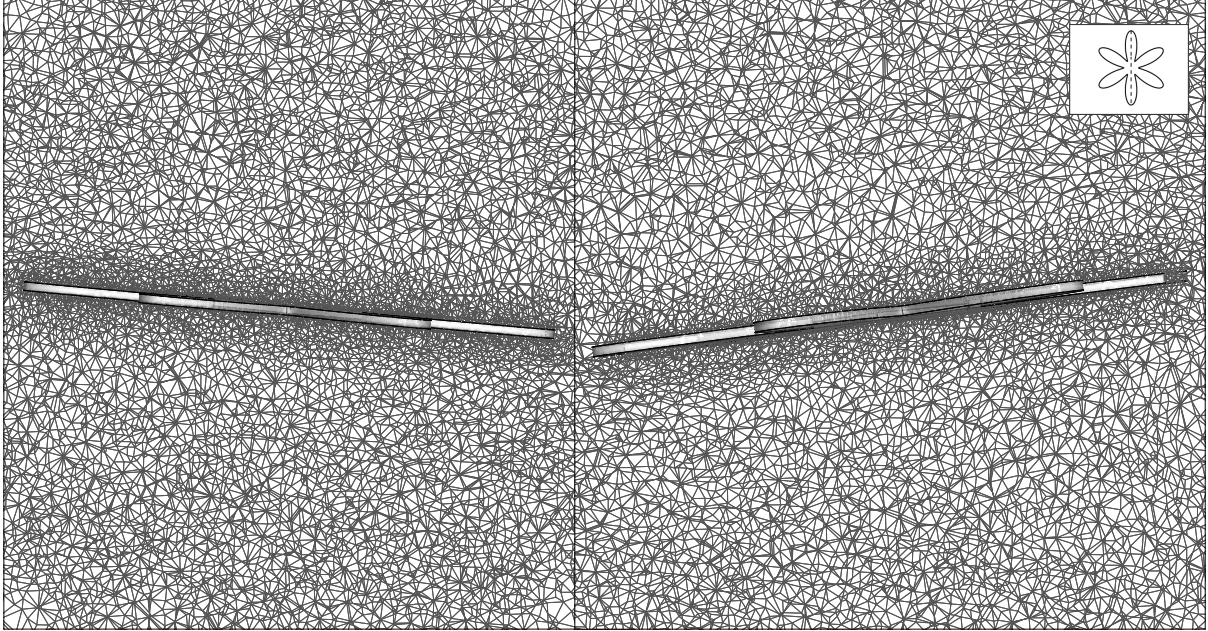
FIGURE 3.2: Example of the dynamic mesh technique applied to two randomly selected snapshots of a 5 mm P1c crystal, demonstrating that the mesh adapts with time to match varying orientations of the crystal.

3.2.2   Mesh

Gridding is completed using ANSYS ICEM CFD meshing software. Stereolithography (STL) faceted geometries are created in AutoCAD using extruded crystal shapes developed using the 'SMOSS' technique laid out in Subsection 2.1.1. The STL files are then loaded into ANSYS ICEM CFD where the computational domain is constructed. The computational domain in this study is spherical, made up of four fluid zones [wind tunnel (WT), sub-wind tunnel (SWT), boundary layer zone (BL), and the sub-boundary layer zone (SBL)] and three boundaries (inlet, outlet, and crystal surface), used to specify boundary conditions (Figure 3.3).
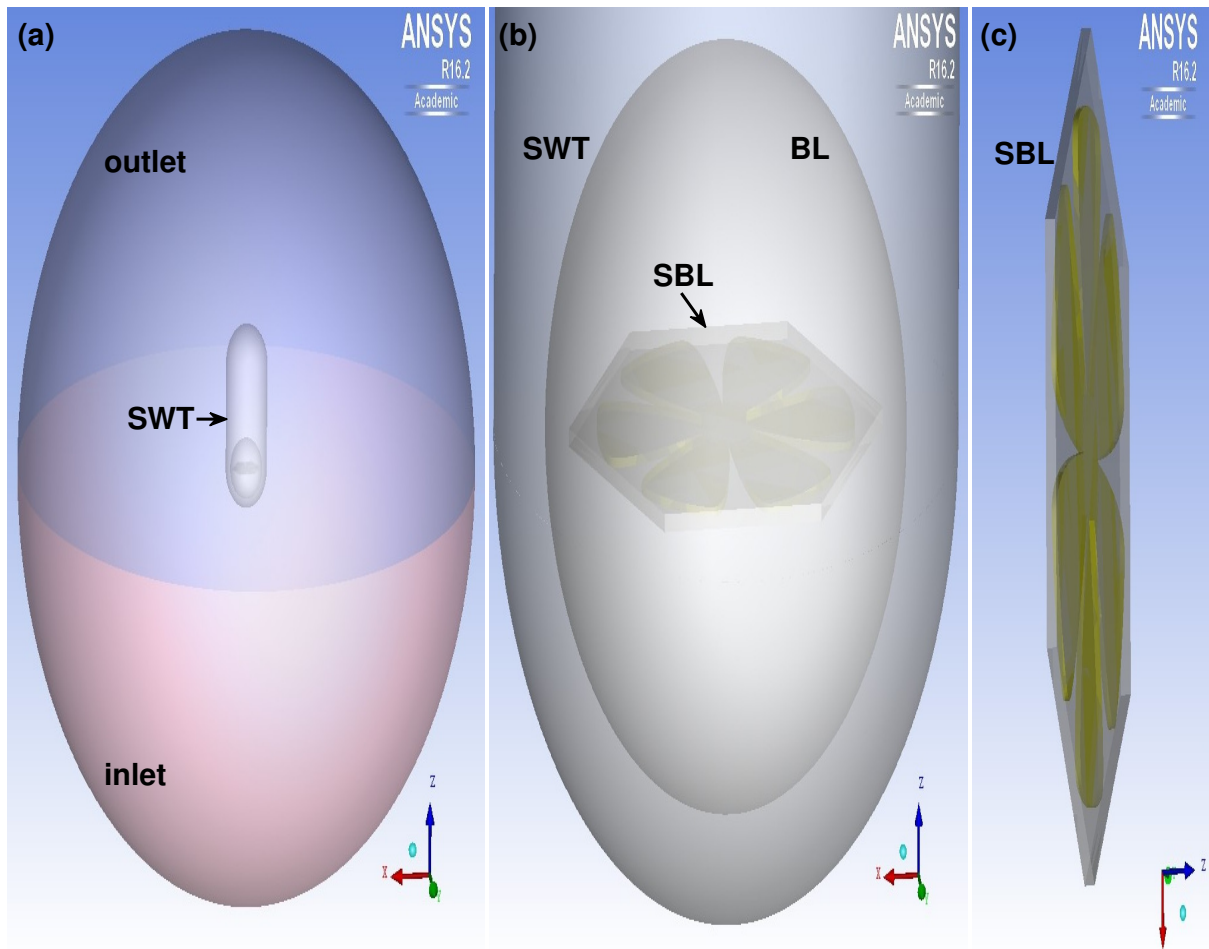
FIGURE 3.3: Definition of computational domain. The spherical domain consists of four fluid zones (WT,SWT,BL, and SBL) and three boundaries (inlet, outlet, and crystal surface). (a) The mesh within WT deforms as SWT moves according to the translational movement of the crystal. (b) The mesh within SWT is not affected by crystal motion. The mesh within BL deforms to account for SBL rotation. (c) SBL moves passively with the crystal, and the mesh contained in the SBL does not change.

The computational domain must be divided in order to constrain the area of the dynamic mesh, and in order to insure adequate mesh quality. The mesh within the WT is allowed to deform to account for movement of the first interior zone, the SWT. The SWT is specified such that it can move according to the translational motion of the ice crystal, but does not rotate. The mesh within the SWT is not affected by the movement of the crystal, and is thus stationary. The BL mesh deforms to account for rotation of the SBL. The SBL moves passively with the ice crystal, inside which the mesh is stationary relative to the crystal. Note, the positions of BL, SBL, and the crystal stay the same relative to SWT.

The WT is spherical with a radius that is 10 times larger than the radius of the ice crystal, with the inlet and outlet spanning the entire lower and upper hemisphere, respectively. The SWT is a cylindrical shape with hemispheric ends. The radius of the cylinder is 1.8 times that of the crystal and the length of the cylinder is 5 times that of the crystal radius. The BL is spherical with radius 1.4 times that of the crystal. The SBL is a hexagonal geometry that fits close to the largest dimension of the crystal. The circle in which the hexagon is inscribed has a radius 1.04 times that of the crystal, and the thickness of the hexagonal region is 1.9 times the thickness of the ice crystal.

The computational domain is discretized with an unstructured tetrahedral grid, which allows precise fitting to the ice crystal shape. The domain consists of about 1.5 - 2.5 $\times$ 10^6 cells (more for larger diameter/smaller aspect ratio). A high density region is imposed

within the SWT, resulting in a mesh that is finer towards the crystal surface and in the

crystal wake and becomes coarser further away from the crystal and wake.

Chapter 4

Results & Discussion

The results of the numerical simulations of freely falling planar ice crystals are presented in this section. Flow fields, fall behavior, velocity, and vapor fields are discussed. While there are 36 cases– four crystal habits, nine diameters– simulated, the results are comparable across different crystal sizes, and thus only a select number of cases are presented as a representation of the results.

4.1 Flow Field & Fall Attitudes

4.1.1 Flow Characteristics

Figure 4.1 shows the pressure distribution and streamlines around four planar ice crystals with Reynolds number near 150 (range 115-175) on the y-z plane for a randomly selected timestep consistent across the each panel. The flows are steady in each case, with a

(a) 2 mm P1b

(b) 3 mm P1c
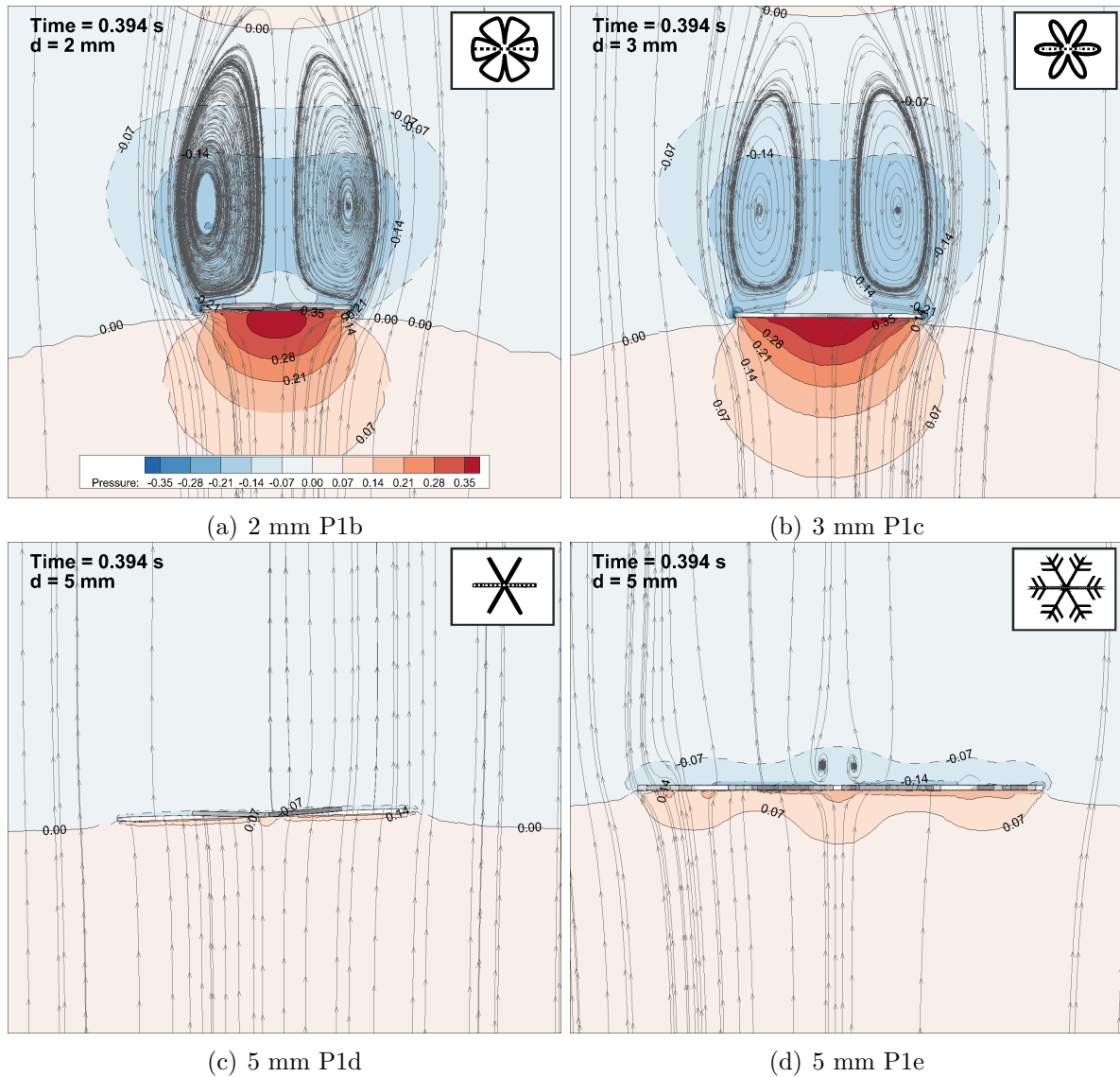
(c) 5 mm P1d

(d) 5 mm P1e

FIGURE 4.1: Pressure deviation (Pa) and streamlines (2D projection onto the central y-z plane) around planar crystals with Reynolds number near 150. Pressure is shown by color shades (red: positive; blue: negative) and contoured (solid: positive; dashed: negative) over a range of -0.35 – 0.35. All snapshots correspond to the same randomly selected timestep.

general left-right symmetry about the central x axis, despite slight rotation about the z axis in many cases. The region of relatively higher pressure in the upstream region is expected, and may work to prevent tiny crystals, droplets, or aerosol particles from colliding with the crystal (Vittori and Prodi, 1967). Standing eddies are present in the wake of the sector plate and broad-branched crystal; the ice plates are falling vertically, while the characteristic of the eddies remain constant. The ice crystals mainly affect the flow within the vertical column in which they fall, only slightly disturbing the area outside this column up to a distance of a few diameters. The results are consistent across the current study for crystals with Re near and less than 100, and is in general agreement with previous studies (e.g. Cheng et al., 2015, Willmarth et al., 1964).

While negative deviations in pressure generally occur in the downstream wake, pressure minima also occur at the upper edge of the plate (Figure 4.2). This behavior is consistent with other numerical studies which treat planar ice crystals as hexagonal plates with finite thickness (two sharp edges), such as Cheng et al. (2015), Hashino et al. (2014), Ji and Wang (1991), Wang and Ji (1997). This configuration of the pressure field at the upper edge of an ice plate likely impacts the collision efficiency, altering the riming rate and the location at which a supercooled drop will strike a plate. This pressure configuration is consistent across all plates in this study.

Figure 4.3 shows the pressure distribution about a 5 mm diameter ordinary dendritic crystal in the y-z plane, offset to see the effect of the thin branches on the pressure field. The same features are observed in this slice as in the central slice, with a high pressure
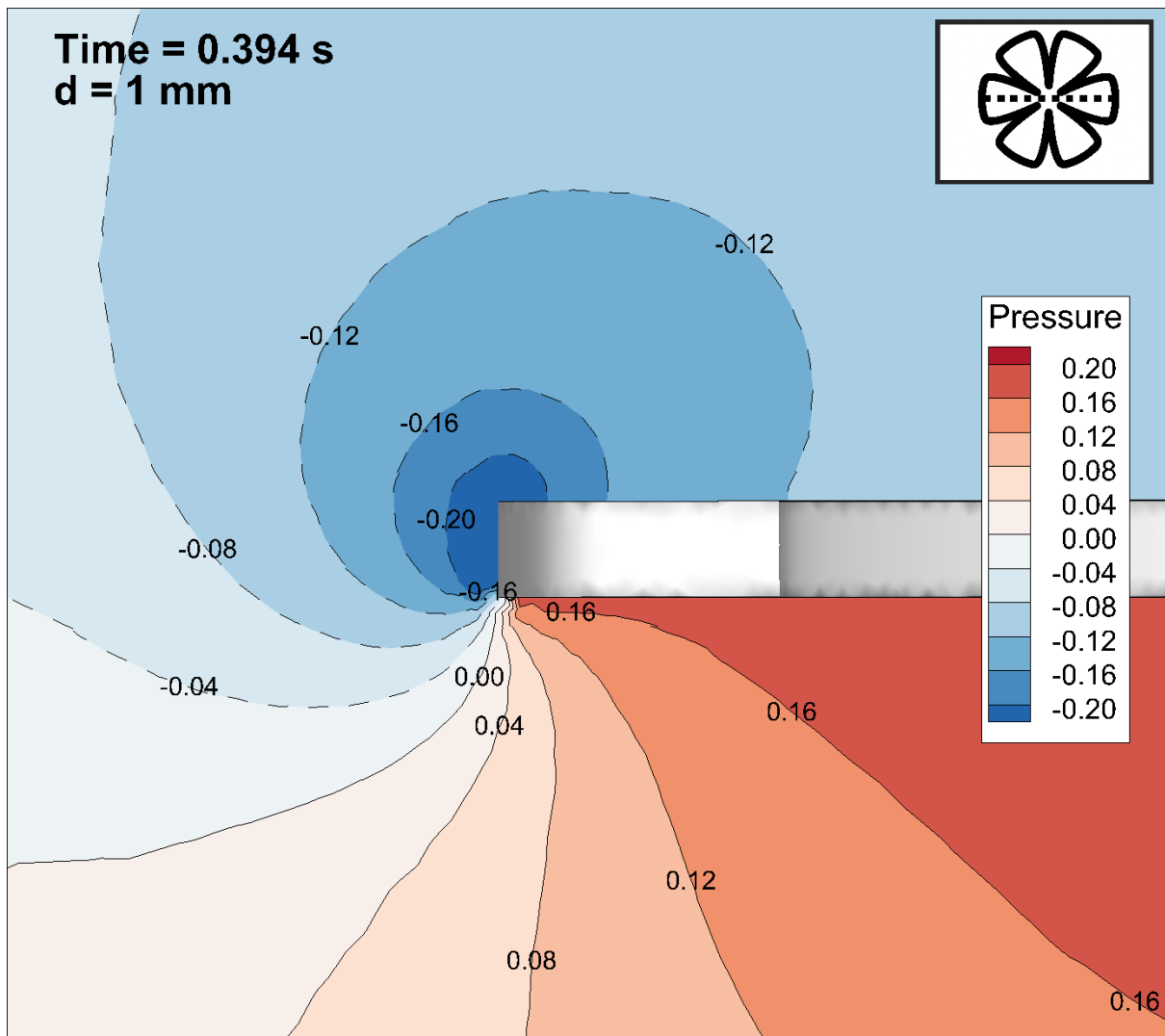
FIGURE 4.2: Pressure deviation (shaded, Pa) around the edge of a 1 mm sector plate with Reynolds number near 40. The time of the snapshot is as in Figure 4.1.

region in the upstream region, and low pressure in the wake. The gaps between the small branches allow the flow to pass through, and the branches themselves have a small radius of influence on the flow. Pressure minima are found along the sharp edges, and in the case of the dendrite, there is ample opportunity for growth along these edges.

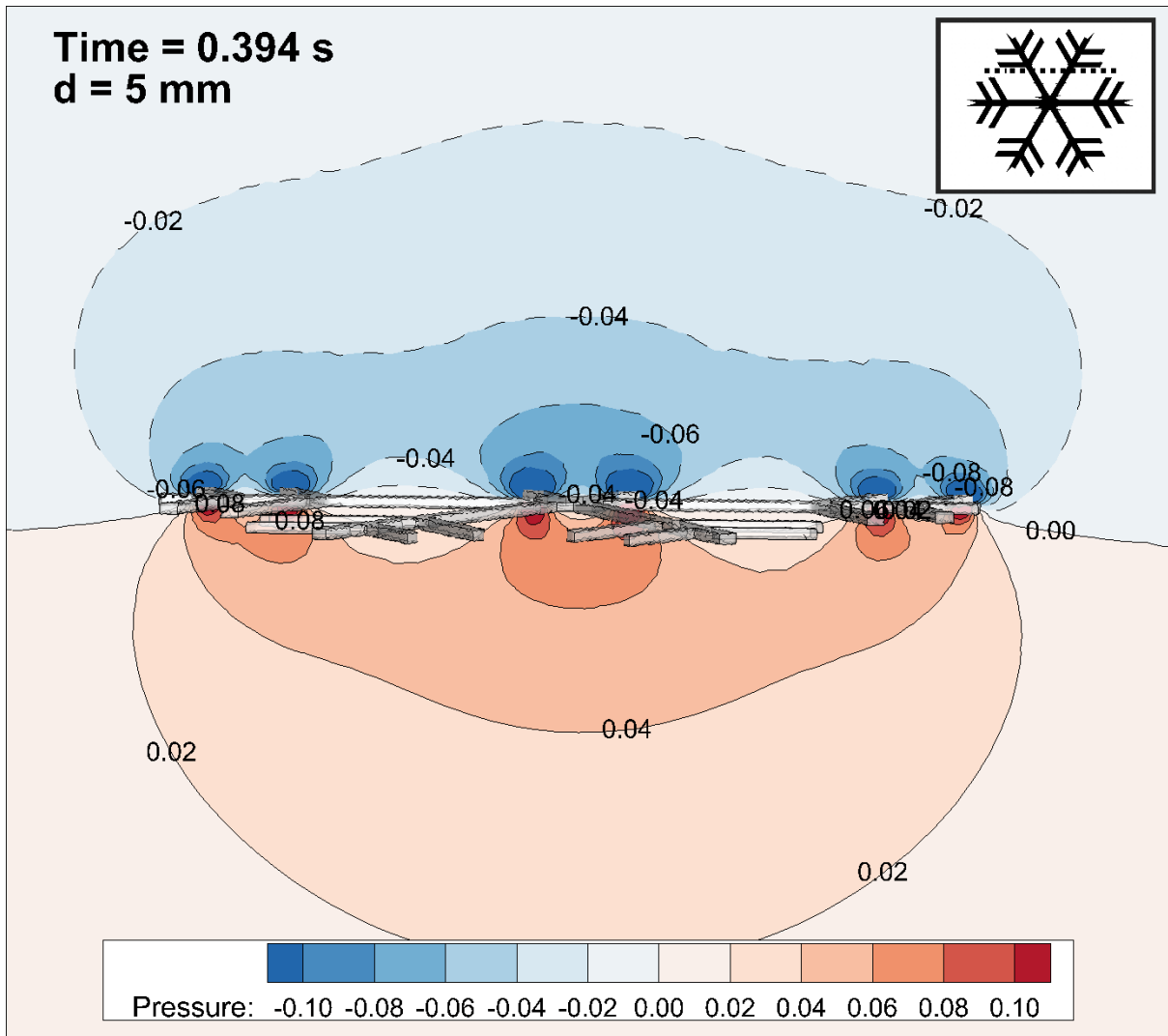As expected, the flow becomes unsteady with increasing Reynolds number (Figure 4.4).

FIGURE 4.3: Pressure deviation (shaded, Pa) around a 5 mm ordinary dendritic crystal with Reynolds number near 175. The 2D slice is slightly off center, revealing the pressure distribution near the small branches of the crystal. The approximate location of the slice is shown in the upper righthand corner. The time of the snapshot is as in Figure 4.1.
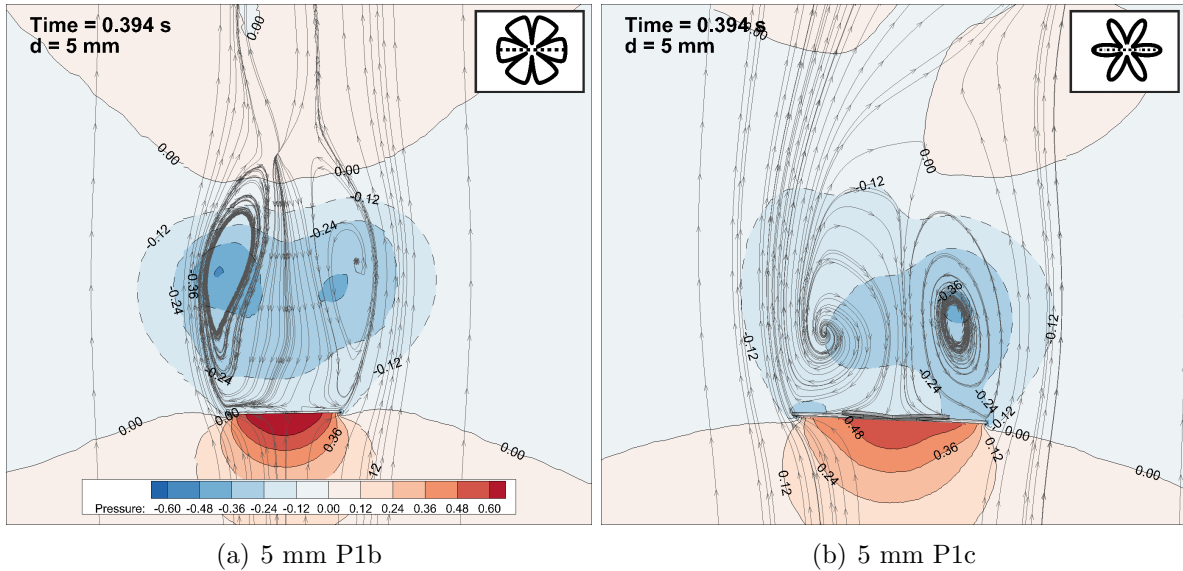
(a) 5 mm P1b (b) 5 mm P1c

FIGURE 4.4: Pressure deviation (Pa) and streamlines (2D projection onto the central y-z plane) around planar crystals with Reynolds number near 350. Pressure is shown by color shades (red: positive; blue: negative) and contoured (solid: positive; dashed: negative) over a range of -0.60 – 0.60. All snapshots correspond to the same randomly selected timestep, as in Figure 4.1.

The stellar crystal and ordinary dendritic crystals do not exhibit unsteady fall behavior over any range of Reynolds number simulated in this study; the sector plate and broad-branched crystal begin to demonstrate unsteady behavior for diameters of 3 mm and above for the sector plate, and 4 mm and above for the broad-branched crystal, corresponding the Reynolds numbers 198 and 258, respectively. Snapshots of a 5 mm diameter sector plate and broad-branched crystal are presented in Figure 4.4. The upstream high pressure region, along with pressure minima along the edge of the crystal surface, are two similarities between the steady cases. The eddies in the downstream wake are no longer symmetric, with eddy shedding occurring in the downstream. Unlike the steady cases in Figure 4.1, the pressure minimum in the wake is not always in contact with the surface

of the plate, but is found slightly above the surface, or in contact with only one region. The pressure minimum changes in both magnitude and location on a near-periodic basis, resulting in eddy shedding. Consistent with Cheng et al. (2015), the location of the upstream pressure maximum is not stationary either, but tends to vary with the orientation of the crystal. As the crystal tilts in a direction, the asymmetric maximum pressure distribution on the underside of the plate will generate a torque, causing the crystal to begin to take on the opposite inclination and move in the opposite direction.
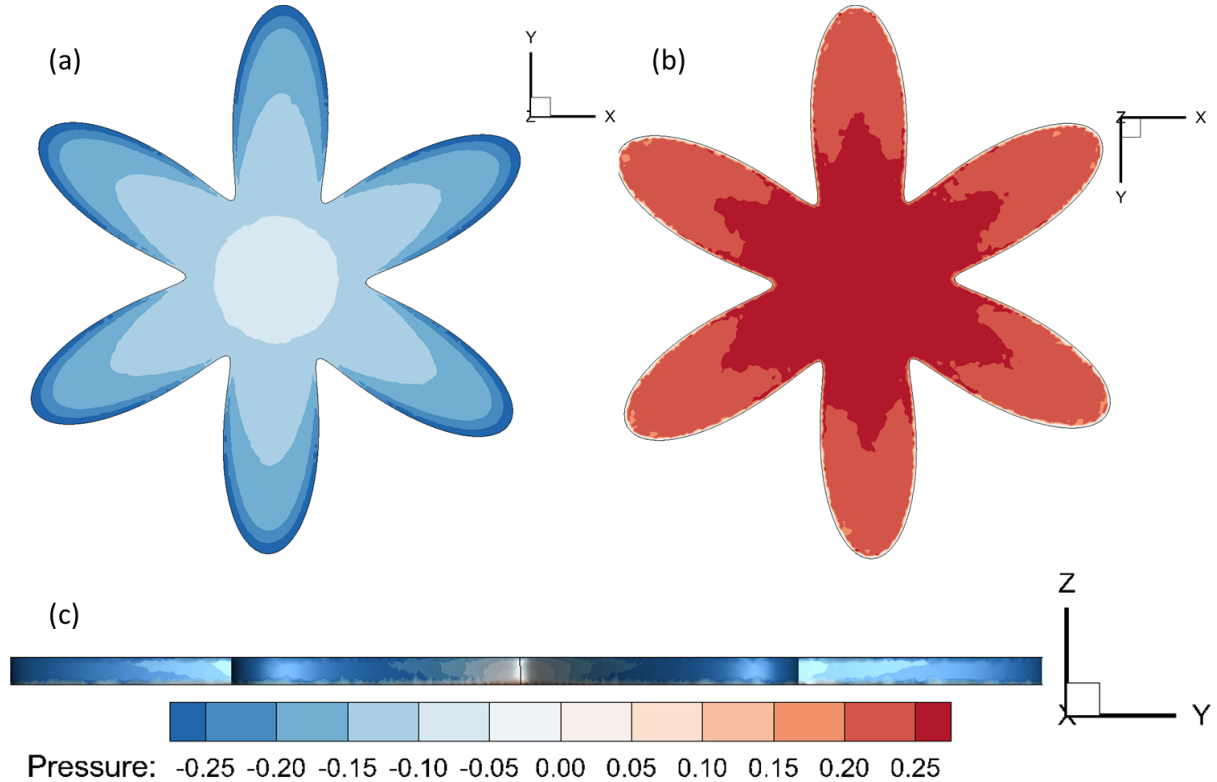

FIGURE 4.5: Pressure deviation (shaded, Pa) on the top (a), bottom (b), and side (c) surfaces of a 2 mm broad-branched crystal with Reynolds number near 95. The time of the snapshot is as in Figure 4.1.

A look at the pressure distribution over the surfaces of a 2 mm broad-branched crystal

is shown in Figure 4.5. Both basal planes are shown as viewed from above and below, along with the edges of the crystal, as viewed from the side. This perspective of the low-pressure side shines light on the location of the pressure minima along the edges seen in the y-z plane slices. Notice that there is not a uniform region of pressure minima along the perimeter of the crystal, rather the minima occur at the peaks of the branches of the crystal and taper off towards the center. This configuration works to explain the process of growth along branches, reproducible in modeling studies (e.g. Gravner and Griffeath, 2009, Pitter and Pruppacher, 1974). The pressure distribution on the surface of the high pressure side of the crystal is more chaotic than the other side. An extremely small sliver of low-to-negative pressure is observed along the entire perimeter of the branches. Finally, the side-view echoes the observations from the basal surfaces; the pressure distribution is such that the minima occur at the peaks, with pressure increasing towards the center of the crystal.

4.1.2 Fall Attitudes

An analysis of the dimensionless displacement, vibration frequencies, and characteristic angles is performed, and the results of each crystal type are presented in Table 4.1. Results are omitted when the vibration frequency or characteristic angles are not obvious or would require subjective interpretation. The vibration frequency about the x and y axis are generally the same, though it is noted when the frequencies differ slightly, and both frequencies are listed for 0.5 mm ordinary dendritic crystal, which differed significantly.

The dimensionless horizontal displacement l^* describes the characteristic length of the horizontal motions relative to the largest dimension of the ice crystal, defined as:

$$l^* = \frac{l}{d}, \qquad (4.1)$$

where l is the length of swing, spiral and irregular motions of the crystal. The dimensionless horizontal displacement of the crystals range from 0.009 to 3.525. In other words, the falling crystals simulated in this study move horizontally with the smallest (largest) distance of 0.9% (353%) of its diameter. The crystal type with the largest range in l^* is the sector plate (P1b); the smallest range in l^* is seen with the stellar crystal (P1d). As in Cheng et al. (2015), no systematic relationship appears to exist between diameter and horizontal dimensionless displacement.

The horizontal motions and orientation of ice crystals may have impacts on the collision efficiency of two crystals. Currently, collision efficiency is defined under the assumption that a collector hydrometeor falls only vertically, ignoring horizontal motions (Pruppacher and Klett, 1997, Wang, 2013). An ice crystal falling with a horizontal component will travel a farther distance than one falling with pure vertical motion, providing more opportunity to collide with small droplets at a different efficiency than the vertically-falling plate. Crystal orientation is important when considering radar backscatter signals from ice plates (e.g., Ishimoto, 2008, Matrosov, 2007).

The Tait-Bryan angles ϕ, θ, and ψ, are used to quantitatively describe the orientation

TABLE 4.1: Dimensionless displacement, vibration frequencies and characteristic angles for the planar ice crystals investigated in this study.

Type	Diameter d (mm)	Dimensionless Displacement l^*	Vibration frequency about x & y axes (Hz)	Characteristic ϕ (°)	Characteristic θ (°)	Vibration frequency about z axis (Hz)	Characteristic ψ (°)
P1b	0.2	3.525	3.66	0.12	0.12	1.22	0.14
	0.3	0.510	25.64	0.30	0.19	12.21	0.05
	0.4	0.052	30.52	0.11	0.04	7.32	0.03
	0.5	1.000	29.30	0.09	0.17	8.55	0.01
	1	0.235	25.64	0.07	0.17	18.81	0.27
	2	0.069	17.09	1.23*	0.24*	—	—
	3	0.826	13.43	1.12	1.49	4.88	0.01
	4	0.115	10.99	2.68	1.17	7.32	0.01
	5	0.263	8.55†	1.77	3.15	23.19	0.27
P1c	0.2	0.043	13.43	0.01	0.01	13.43	0.03
	0.3	0.015	4.88	0.02	0.02	3.66	0.12
	0.4	0.761	1.22	0.16	0.09	4.88	1.16
	0.5	2.466	1.22	0.09	0.11	3.66	0.07
	1	0.015	24.41	0.01	0.04	—	—
	2	0.009	19.53	0.01	0.01	—	—
	3	0.012	14.65	0.24*	0.28*	—	—
	4	0.054	12.21	0.88	0.29	1.22	0.08
	5	0.052	10.99	4.30	1.97	1.22	3.45
P1d	0.2	0.059	—	—	—	14.65	0.00
	0.3	0.274	3.66	0.39	0.82	1.22	0.03
	0.4	0.199	3.66	0.58	0.44	25.64	0.01
	0.5	0.217	3.66	0.23	0.42	8.55	0.01
	1	0.141	10.99	0.07	0.13	3.66	0.14
	2	0.162	4.88	0.14	0.21	—	—
	3	0.310	3.66†	0.01	0.59	—	—
	4	0.121	3.66	0.96	0.30	3.66	0.02
	5	0.227	3.66	0.57	0.53	—	—
P1e	0.2	0.060	4.88†	0.09	0.04	10.99	0.02
	0.3	0.554	1.22	0.09	0.06	—	—
	0.4	0.796	7.32	0.04	0.06	—	—
	0.5	0.415	1.22/4.88	0.08	0.15	8.55	0.01
	1	0.293	3.66†	0.00	0.02	—	—
	2	0.120	10.99	5.32‡	1.06‡	3.66	8.38
	3	0.144	7.32†	1.92‡	3.77‡	3.66	3.16
	4	0.047	4.88	0.04	0.06	—	—
	5	0.044	4.88§	0.03	0.01	—	—

*Amplitude shows an increasing trend with time, may be underestimated.
†The vibration frequency about the x axis is slightly larger than the y axis.
‡Amplitude shows a decreasing trend with time, may be overestimated.
§The vibration frequency about the y axis is slightly larger than the x axis.

of the ice crystals with respect to their initial orientation (Table 4.1). The angles ϕ, θ, and ψ are defined and correspond to rotation about the x, y, and z axes of the crystal, respectively. The characteristic angle and vibration frequency results are confirmed using supporting evidence from performing a fast Fourier transform (FFT) of the orientation data. The vibration frequency about the z axis have been omitted when the high-frequency signal was not obvious compared to the low-frequency signal.

Figure 4.6 shows the time-varying Tait-Bryan angles for a 3 mm broad-branched crystal (P1c). The rotation around the x and y axes (ϕ, θ) show periodic behavior, oscillating at

the same frequency (14.65 Hz), appear anti-phased, and have amplitudes which increase with time. The low-frequency signal of the vibration frequency about the x axis is well demonstrated. This is an example of a case in which the smaller amplitude, high frequency signal is not obvious.
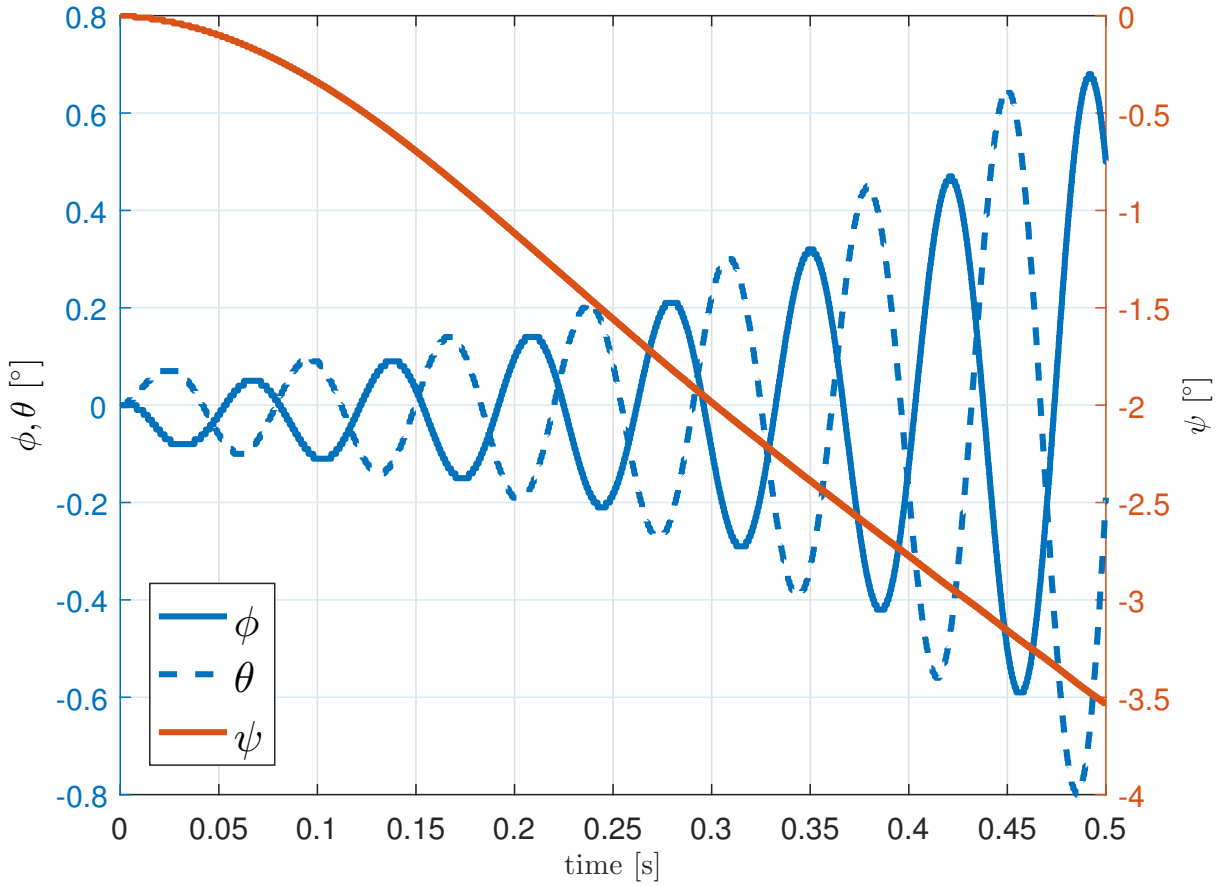

FIGURE 4.6: Tait-Bryan angles ϕ, θ, and ψ of a falling 3 mm broad-branched crystal (P1c) as a function of time.

Rotation about the z axis is observed with the small, steady state crystals, though the characteristic angles are generally order 10^{-1} or 10^{-2} degrees. Nothing in principle should cause spinning in the steady cases of the idealized crystals. This behavior likely arises from slight imperfections in the meshing processes, which causes inevitable asymmetry.

Lack of exact symmetry of the mesh and crystal, leading to an uneven distribution of mass, is a possible explanation for some crystal cases demonstrating oscillation about a preferential a axis, even though the moments of inertia about any a axis are the same.

Figure 4.7 shows the fall patterns of each crystal type with Reynolds number Re of order 10, visualizing the x-z plane trajectories. The starting positions, with no initial inclination angle, are shown by the projections highlighted in green; the end positions, occurring at 0.5 s, are shown by the red highlighted projections. The projections are displayed every 0.005 s. Generally, any early oscillation of the crystal, caused by being subjected to an initial flow, is damped quickly for most crystal types, the exception being the stellar crystal, which continues to fall with a slight orientation of around -0.65° after 0.2 s. The broad-branched crystal exhibits the largest horizontal displacement relative to its diameter, 247%; the horizontal dimensionless displacements for the sector plate, stellar, and ordinary dendritic crystals in Figure 4.7 are 5%, 14%, and 29%, respectively. The velocity of the crystal relative to the base flow (a first approximation of the terminal velocity) can be inferred by the distance between projections. The sector plate, with Re = 12, demonstrates a reduction in velocity relative to the flow. When initially perturbed, the broad-branched crystal falls quicker, relative to the flow, because of the reduction in surface area exposed to the flow, also leading to a horizontal translation.

The x-z plane trajectories for crystals with Reynolds number near 350 are shown in Figure 4.8. These cases are less stable with time, and appear quite unstable towards the end
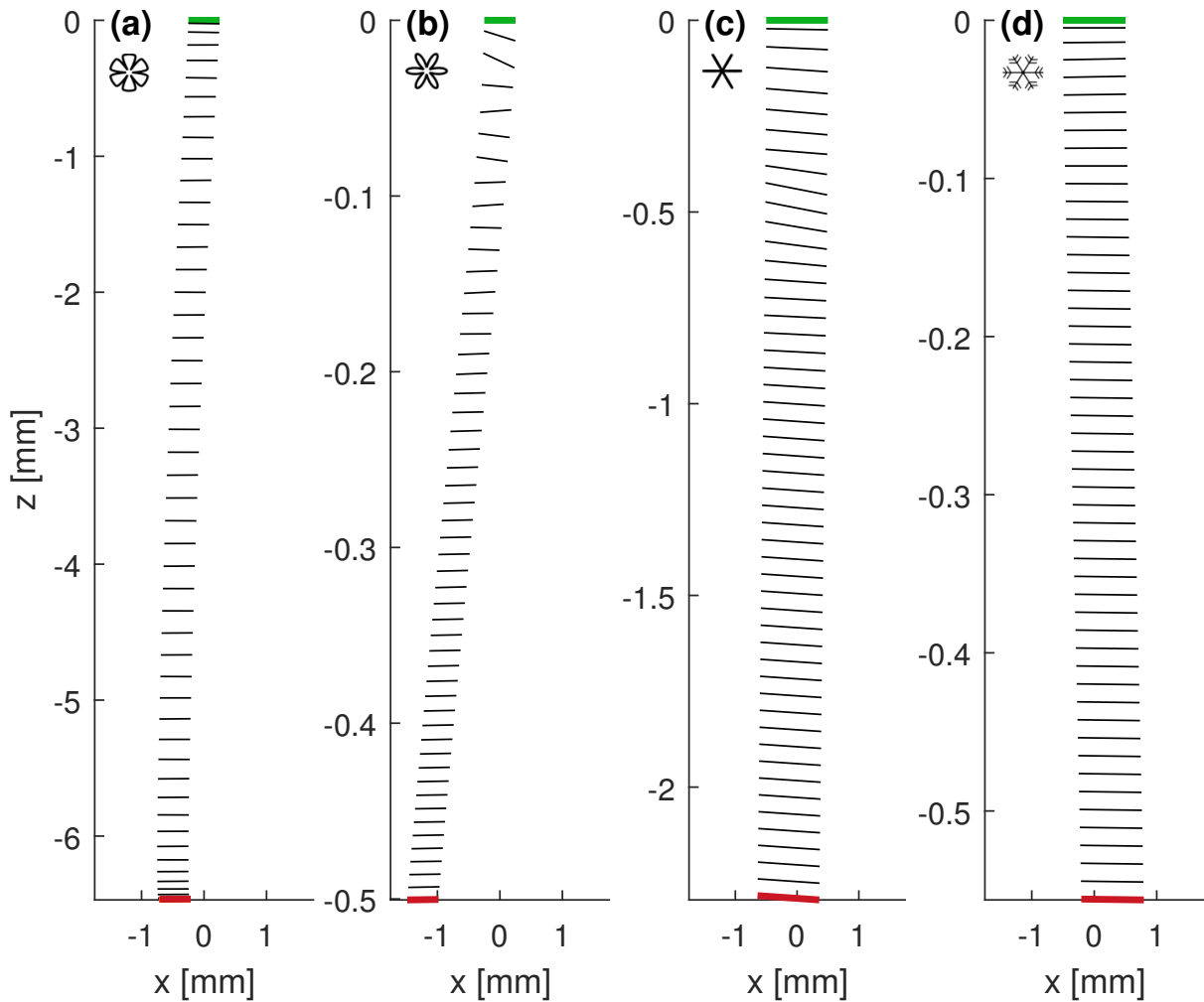
FIGURE 4.7: Fall trajectories of planar ice crystals as shown through consecutive snapshots of the crystal position on the x-z plane for (a) sector plate (P1b), Re = 12; (b) broad-branched crystal (P1c), Re = 9; (c) stellar crystal (P1d), Re = 7; and (d) ordinary dendritic crystal (P1e), Re = 14. The time interval is 0.005 s. The initial (final) position of the crystal is highlighted green (red) on the projection.

of the simulation time. The zigzag swing oscillations in the sector plate result in horizontal translations of roughly 26% of diameter of the plate; fluttering in the broad-branched crystal produces a smaller horizontal displacement of 5% of its diameter. Intuitively, the crystal is displaced rightward (leftward) horizontally in response to tilting to the right (left), in agreement with experimental results of Willmarth et al. (1964) and Stringham et al. (1969) and consistent with the numerical results of Cheng et al. (2015) and Hashino et al. (2016).

Crystal fall behavior and fall velocity are contributing factors for understanding the aggregation process of snow crystals (e.g., Sasyo, 1971). An observational study by Kajikawa (1992) showed a relationship between increasing Reynolds number, above about 40, and unstable falling motion due to vortex shedding. In that study, unstable falling motion first began with oscillations about an a-axis of plate-like crystals, then proceeded to display swinging motion, followed by rotation about the z axis, with increasing Re. Note, tumbling motions that were observed in tank experiments by Willmarth et al. (1964) and Stringham et al. (1969) were not observed in the Kajikawa (1992) observational study. Further, due to natural snow crystal asymmetry, the onset of observed unstable falling motion in the Kajikawa (1992) study occurred at considerable smaller Re values than in model experiments (e.g., List and Schemenauer, 1971). In the current CFD model experiment, the onset of unstable fall motion did not occur until higher Re, with the highest Re for stable motion occurring at Reynolds numbers 115 and 175 for the simulated sector plate and broad-branched crystal, respectively; the stellar crystal and ordinary dendritic crystal exhibits stable falling motion for all Re considered in this study. For comparison,
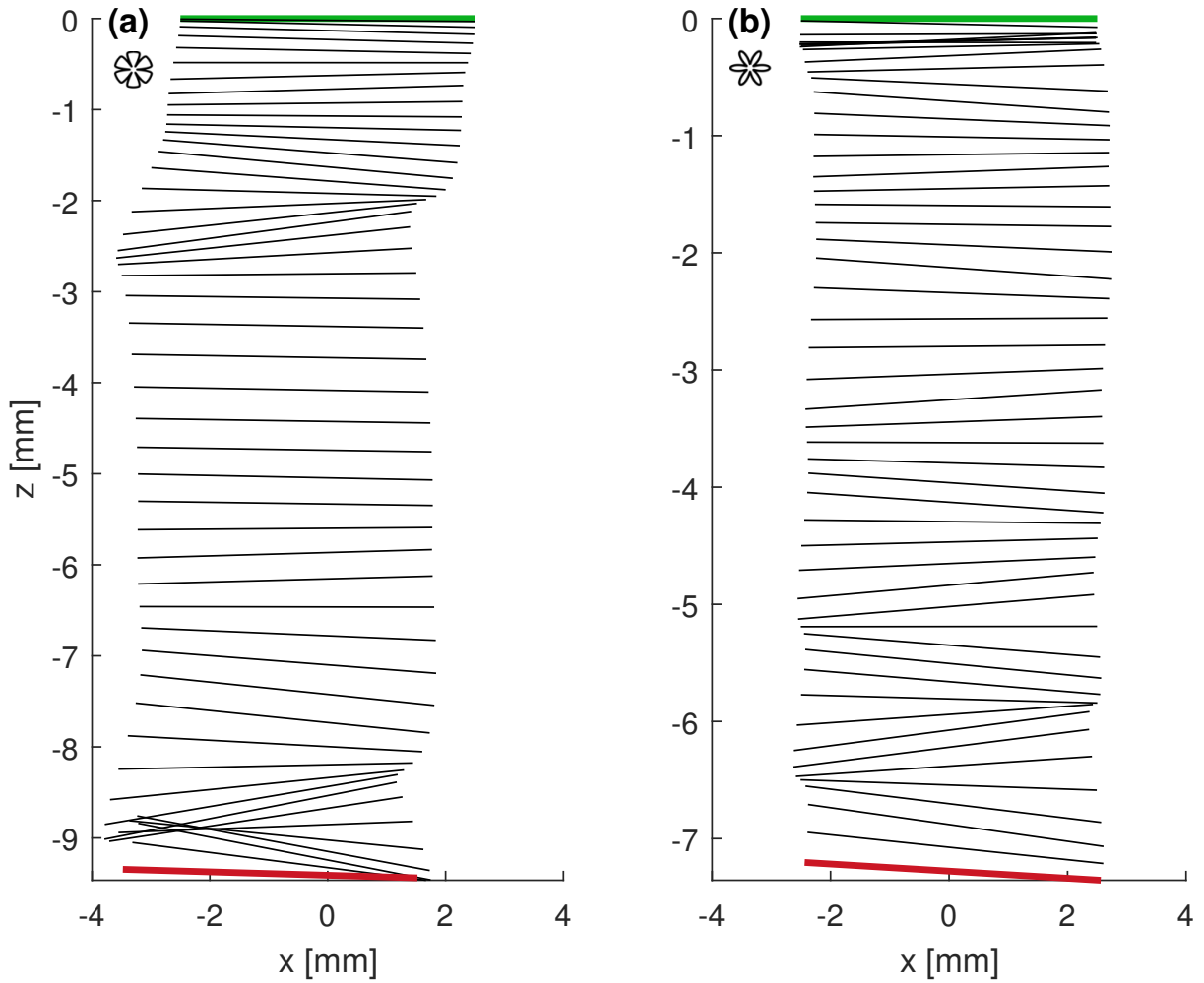
FIGURE 4.8: Fall trajectories of planar ice crystals as shown through consecutive snapshots of the crystal position on the x-z plane for (a) sector plate (P1b), Re = 384; and (b) broad-branched crystal (P1c), Re = 345. The time interval is 0.005 s. The initial (final) position of the crystal is highlighted green (red) on the projection.

the highest Re for stable disk motion in the Willmarth et al. (1964) tank study was 172. In that study, tumbling motions only occurred for Re in excess of 2000, much larger Re than those observed in the current study.

For plate-like crystals, Kajikawa (1992) showed that the limit of the onset of unstable
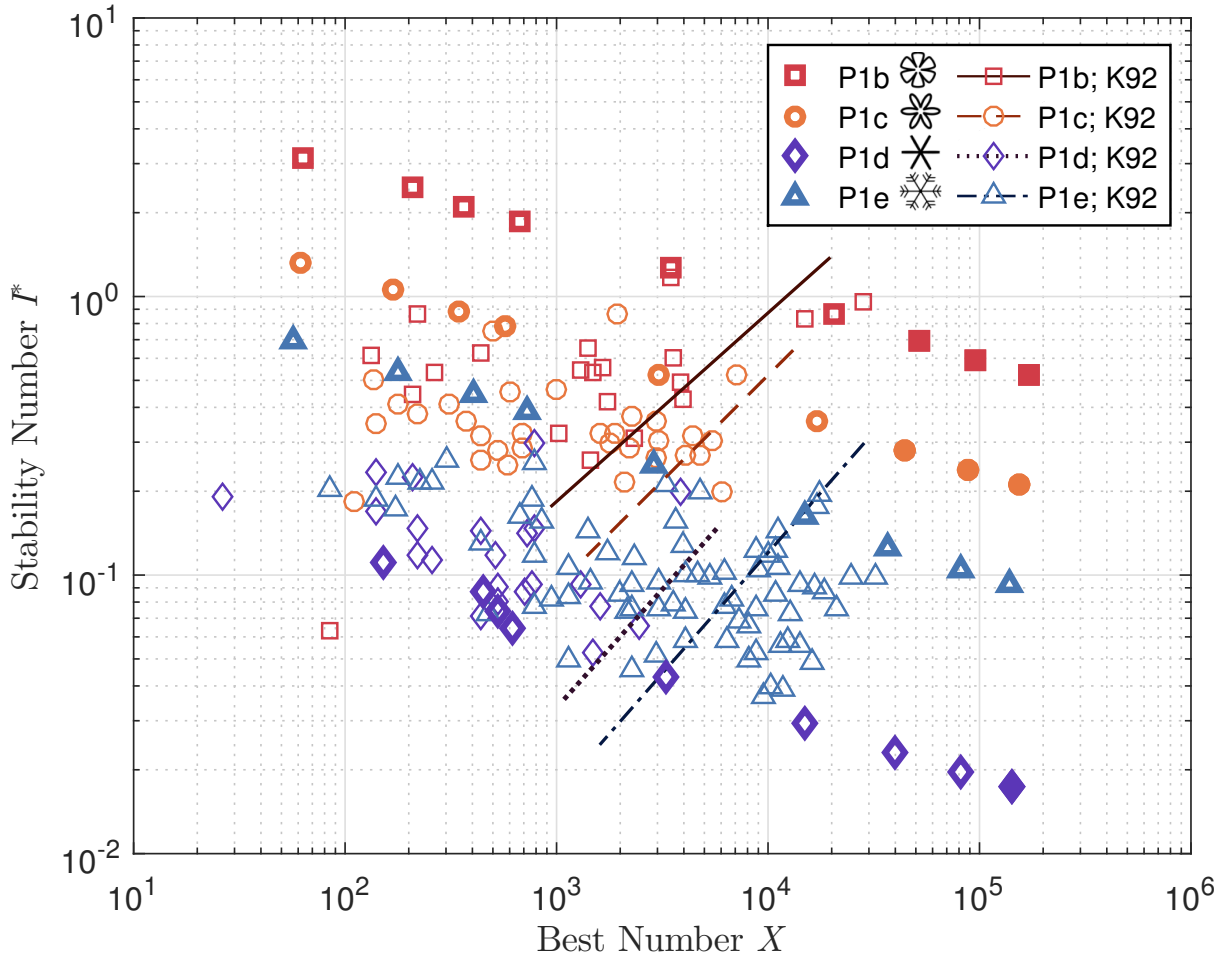
FIGURE 4.9: Stability number against Best number of planar crystals. Emphasized boldface square, circle, diamond, and triangle markers indicate the results for: sector plates (P1b), broad-branched crystals (P1c), stellar crystal (P1d), and ordinary dendritic crystals (P1e), respectively. Filled markers indicate cases exhibiting unstable fall behavior. The results of Kajikawa (1992) are indicated by thin shapes of the respective type and corresponding color. Curves indicate the approximate boundary between stable (northwest of line) and unstable (southeast) falling motions, also from Kajikawa (1992): solid curve for sector plates, dashed curve for broad-branched crystals, dotted curve for sector plates, and dash-dot curve for dendrites.

falling motion is better determined by the Best or Davies number ($X = C_D Re^2$) and dimensionless moment of inertia, or stability number ($I^* = {}^{I_a}/_{\rho d^5}$, Equation 2.7). Kajikawa (1992) approximated the plate-like crystals as hexagonal plates in the calculation of I_a and X, whereas this study performs those calculations without such an approximation. Figure 4.9 investigates the relationship between stability number and Best number, including I^* and X data from the current study (emphasized data points, filled markers when exhibiting unstable, swinging motions), along with data from previous studies by Kajikawa, presented in Figure 4 of Kajikawa (1992). The boundaries between stable (left of line) and unstable (right of line) from Kajikawa (1992) are given by the solid lines corresponding to the crystal type of that color. Crystals with larger surface area exposed to the flow are characterized by larger stability number. Unstable fall behaviors occur at higher X in the current study compared to Kajikawa (1992) as explained above. Dendritic crystals, which have large internal ventilation, fall in a stable manner over a larger range of X, suggesting falling motion stability is influenced by the internal ventilation of crystals (Kajikawa, 1992).

4.1.3   Vorticity

The vorticity magnitude distributions on the cross section through the center of falling 5 mm sector plate and ordinary dendritic crystal are shown in Figure 4.10. As expected, the maximum in the vorticity magnitude is observed at the edges of the crystal, where the flow is changing direction and speed. The vorticity is transported downstream by the flow, with higher vorticity forming a champagne glass-shape, with the center void of

high vorticity for the sector plate. The vorticity is advected downstream for the dendrite as well, not only at the outer edges, but at the interior edges as well. The vorticity is advected further downstream in the 5 mm sector plate wake than the dendrite, due to the difference in the speed of the flow–terminal velocity of 1.08 m s^{-1} and 0.49 m s^{-1} for the plate and dendrite, respectively. The interior of the wake in the sector plate contains a region of low vorticity (less than 100 s^{-1}) located slightly above the surface of the crystal, appearing in a random pattern.
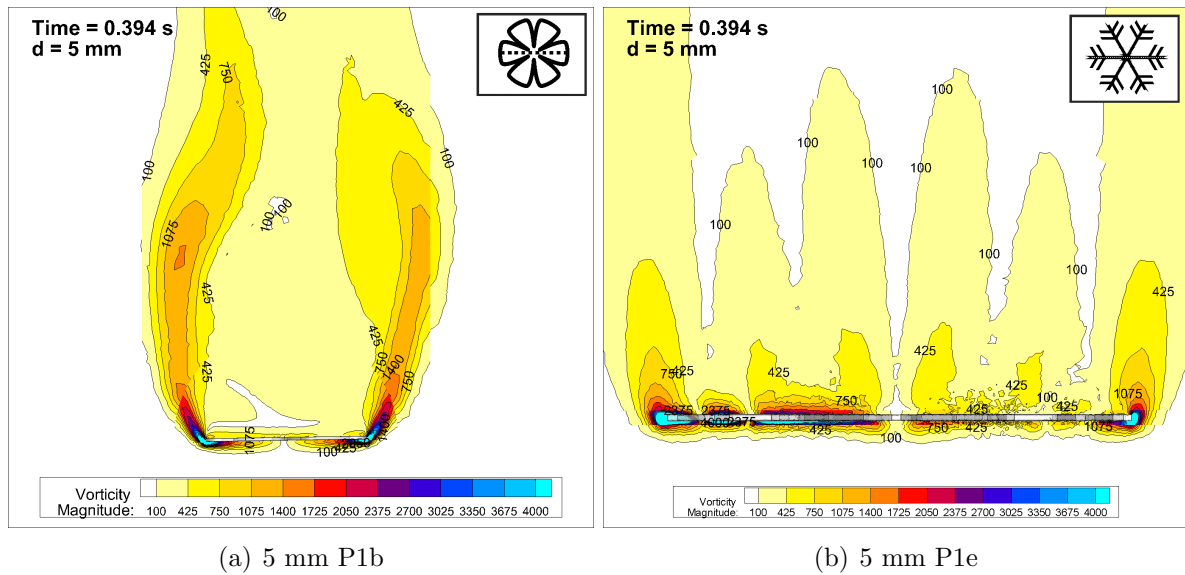

(a) 5 mm P1b   (b) 5 mm P1e

FIGURE 4.10: Vorticity distribution (s^{-1}) around a sector plate (a) and ordinary dendritic crystal (b). Vorticity magnitude is shown by color shades (yellow: low; bright blue: high) over a range of 100 – 4000 s^{-1}. The snapshots correspond to the same randomly selected timestep, as in Figure 4.1.

The vorticities form intertwining vortex tubes in the downstream wake, shown in Figure 4.11 as 3D $\hat{z}$-vorticity isosurfaces of ± 400 s^{-1}. This structure may impact the collection of small cloud particles with subsequent ice crystals downstream by chaotically redistributing the particles in space. The positive/negative alternating pattern of the
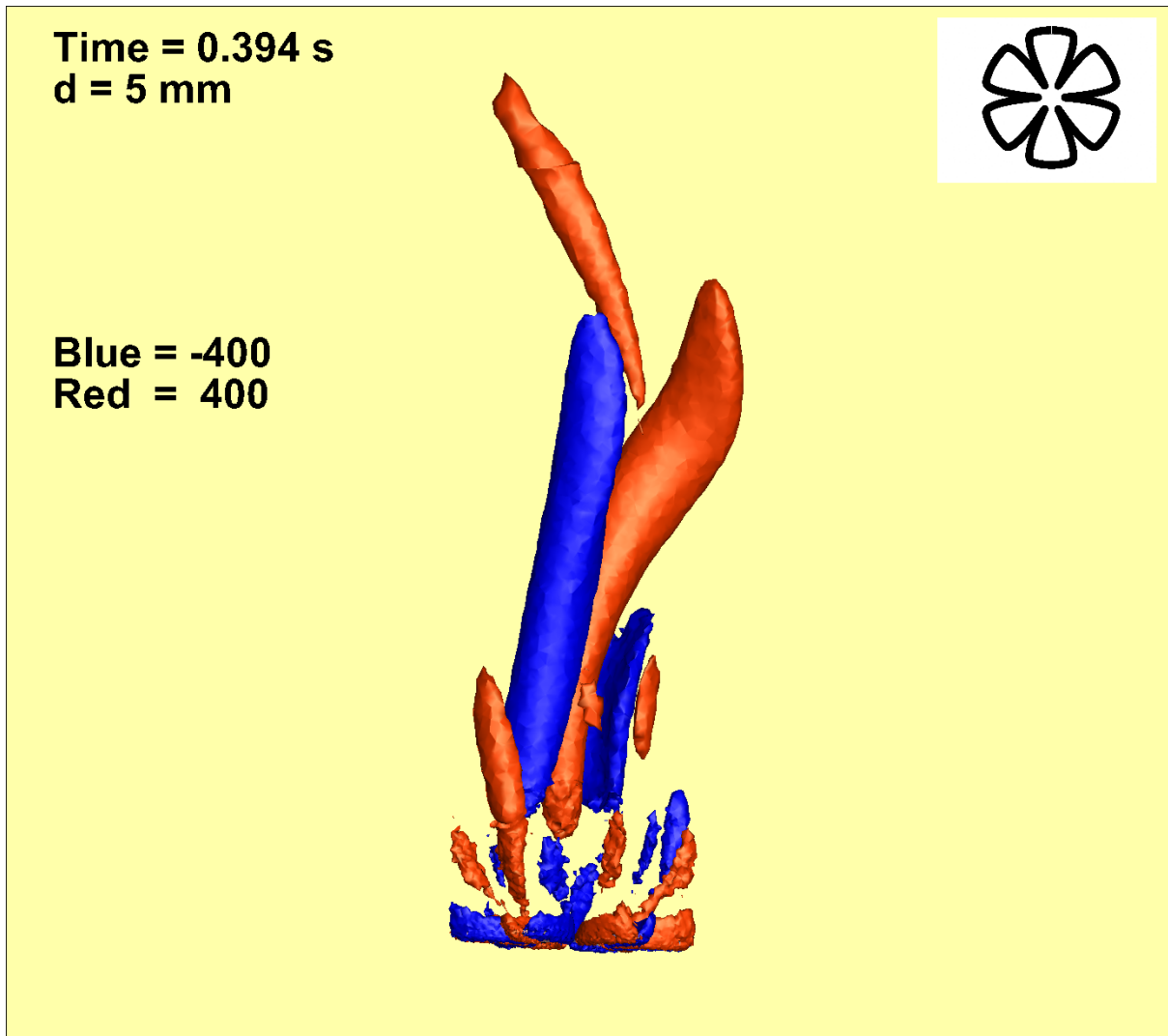
FIGURE 4.11: 3D $\hat{z}$-vorticity isosurface (s^{-1}) around a 5 mm sector plate to illustrate the unsteady vortex structure. The blue isosurfaces correspond to $\hat{z}$-vorticity values of -400 s^{-1} while the red isosurfaces correspond to $\hat{z}$-vorticity values of 400 s^{-1}. The snapshot corresponds to the same randomly selected timestep, as in Figure 4.1.

vorticity isosurfaces around the sector branches is intuitively understood considering the direction in which the flow will curl on either side of the branch.

The flow fields and fall attitudes discussed above are in general agreement with previous studies (e.g. Cheng et al., 2015, Willmarth et al., 1964). Features, such as the pressure minimum on the upper edge of the peaks of the ice plate, is prevalent in all cases, and lends support to the observation that crystals tend to grow faster about their peaks. Projections of the fall attitudes of crystals at varying Reynolds number, along with an analysis of the characteristic angles, may be of use for the cloud modeling community.

4.2   Terminal Velocity & Drag Coefficients

4.2.1   Terminal Velocity

Consistent with the findings of Cheng et al. (2015), the results of this study show that the terminal velocity of simulated ice crystals fluctuate throughout the fall process, generally bound within a certain range. The range is smaller for crystals which fall with the basal plane entirely normal to the fall direction, likely because the cross-sectional area exposed to the flow is nearly constant. The range is larger for crystals exhibiting swinging, unstable motion, because with an inclination relative to the flow, the implied smaller cross-sectional area decreases the upward drag force and increases the downward acceleration. The velocity relative to the flow initially varies from case to case as the crystal responds to the first approximation base velocity to which it is subjected. For this reason, the terminal

velocity is computed by averaging the last 3000 time steps of the simulation, as per the method outlined in Cheng et al. (2015).
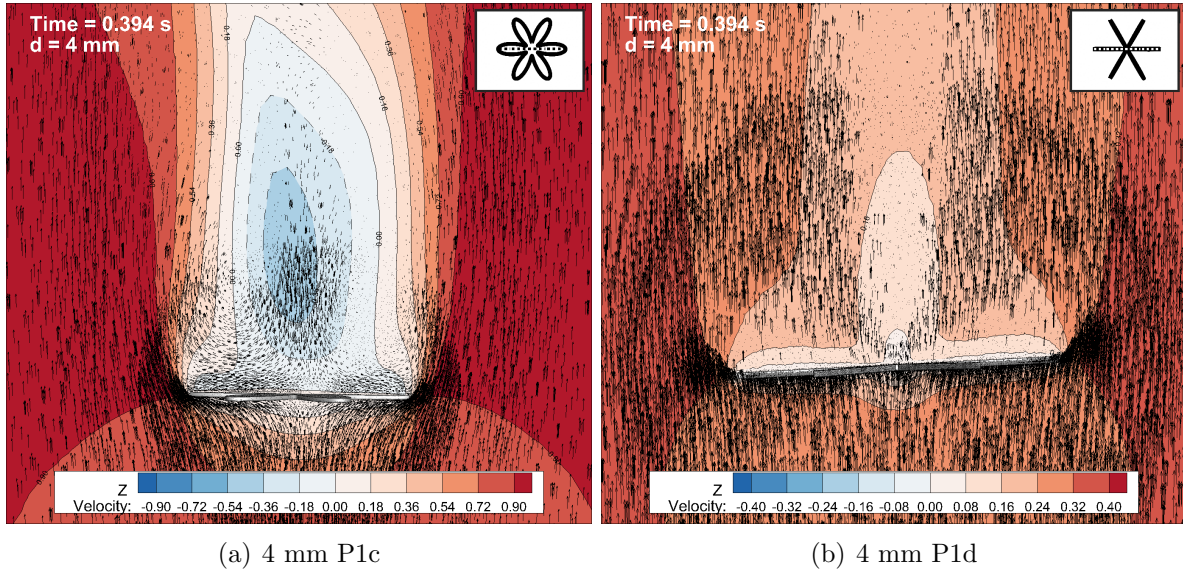

(a) 4 mm P1c

(b) 4 mm P1d

FIGURE 4.12: $\hat{z}$-velocity (m s^{-1}) and velocity vector (2D projection of the 3D vector onto the central y-z plane) around a broad-branched (a) and stellar crystal (b). $\hat{z}$-velocity is shown by color shades (red: positive; blue: negative) over a range of -0.40 – 0.40 m s^{-1}. The snapshots correspond to the same randomly selected timestep, as in Figure 4.1.

Figure 4.12 shows the $\hat{z}$-velocity distribution and velocity vectors around a 4 mm broad-branched crystal and stellar crystal. Note the scales are panel-specific, corresponding to the calculated terminal velocity for each crystal, 91.0 cm s^{-1} and 32.5 cm s^{-1}, respectively. Note that the velocity vectors are projections of the 3D vectors onto the y-z plane crossing the center of the plate, thus not all vectors are on the same plane, and the uneven vector distribution is explained by the non-uniform mesh used to conform to the surface of the crystal and to allow for mesh adjustment with time. At distances sufficiently far from the crystal, the velocity nears the initial condition terminal velocity estimation at which the

crystals are subjected during the simulation. Due to the no-slip condition, the fluid is stagnant everywhere on the solid crystal surface. Both crystals have areas of low velocity from the high pressure on the underside of the crystal ("front stagnation" region); the area of lower velocity is larger, relative to the diameter, for the broad-branched crystal than the stellar crystal (Re 260, 89, respectively). The broad-branched crystal displays a region of negative velocity, or return flow/recirculation, in the wake, as opposed to the stellar crystal, with lower Reynolds number. There is a degree of symmetry to both velocity fields, though the wake of the broad-branched crystal shows slight oscillation of the velocity magnitude at a distance of about 4 mm above the surface of the crystal. The velocity gradient near the crystal surfaces–and in the case of the 4 mm broad-branched crystal, in the wake as well–implies the vorticity will be large here.

Figure 4.13 presents the terminal velocity for each crystal type in this study, alongside the numerical results of the hexagonal plate *P1a* from Cheng et al. (2015) and the observational parameterizations of Heymsfield and Kajikawa (1987) for the corresponding crystal type. The terminal velocity increases with increasing diameter, consistent with the observational data and previous numerical results. For the sector plates, broad-branched crystals, and ordinary dendritic crystals investigated in this study, the terminal velocities are greater than those of the observational ones, likely because the mass of the idealized crystals represent the upper bound for that of natural crystals, as discussed previously. The simulated stellar crystals have terminal velocities consistently lower than those of the observational results of Heymsfield and Kajikawa (1987) for a given diameter; Heymsfield and Kajikawa (1987) observations may encompass a spectrum of "stellar" shapes,
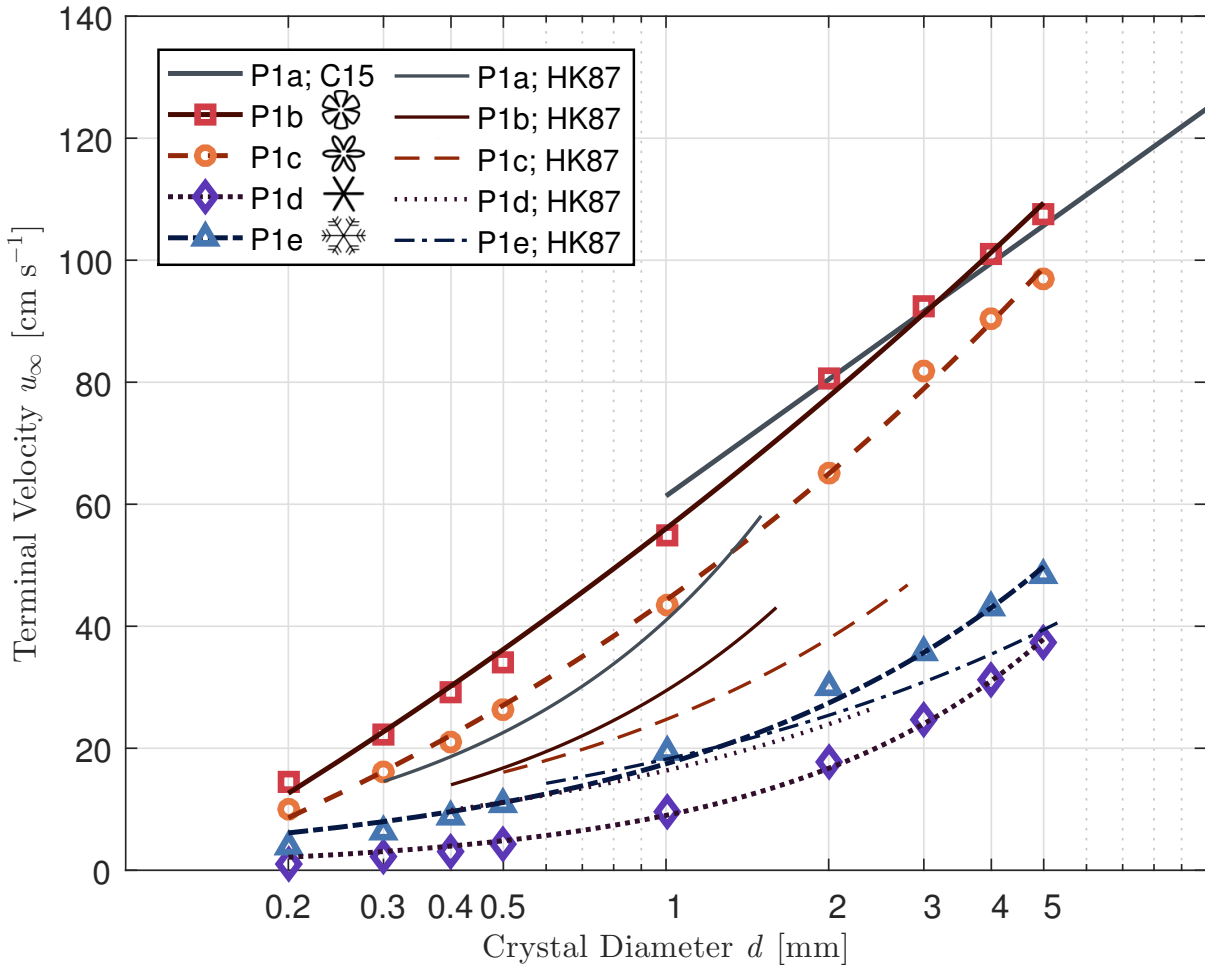
FIGURE 4.13: Terminal velocities (cm^{-1}) of planar crystals. Square, circle, diamond, and triangle markers indicate the results for: sector plates (P1b), broad-branched crystals (P1c), stellar crystals (P1d), and ordinary dendritic crystals (P1e), respectively. The corresponding bold curves are the power law fits given by Equations (4.2) to (4.5): solid curve for sector plates, dashed curve for broad-branched crystals, dotted curve for sector plates, and dash-dot curve for dendrites. Thick, grey, solid curve represents the parameterization of hexagonal plates from Cheng et al. (2015). The corresponding parameterizations of Heymsfield and Kajikawa (1987) are shown by thin curves, with colors and line styles matching these experimental results.

whereas the calculated values in this study are from idealized shapes.

The calculated terminal velocities u_∞ of each crystal type can be fit by the following power law relationships:

$$\text{Sector plates: } u_\infty = 9.507 \times 10^{-1}\, d^{0.1289} - 1.756, \tag{4.2}$$

$$\text{Broad-branched crystals: } u_\infty = 1.673 \times 10^{-1}\, d^{0.2635} - 0.5899, \tag{4.3}$$

$$\text{Stellar crystals: } u_\infty = 1.872 \times 10^{-4}\, d^{0.8939}, \tag{4.4}$$

$$\text{Ordinary Dendritic crystals: } u_\infty = 1.944 \times 10^{-3}\, d^{0.6511}, \tag{4.5}$$

where u_∞ has units of meters per second and d is in microns. The root-mean-square error of the fits are 0.020, 0.017, 0.008, and 0.017 m s^{-1}, respectively. The relationships are valid over the range of diameters studied, 200 μm to 5000 μm.

4.2.2   Drag Coefficient

Figure 4.14 shows the time-averaged drag coefficient as a function of Reynolds number, where the C_D has been computed as the average C_D over the last 3000 time steps, as described above. Drag coefficient data from other studies is presented in the figure for comparison, including numerical results for hexagonal plates *P1a* from Cheng et al. (2015), Hashino et al. (2014), Wang and Ji (1997) and for broad-branched crystals, also from Wang and Ji (1997).
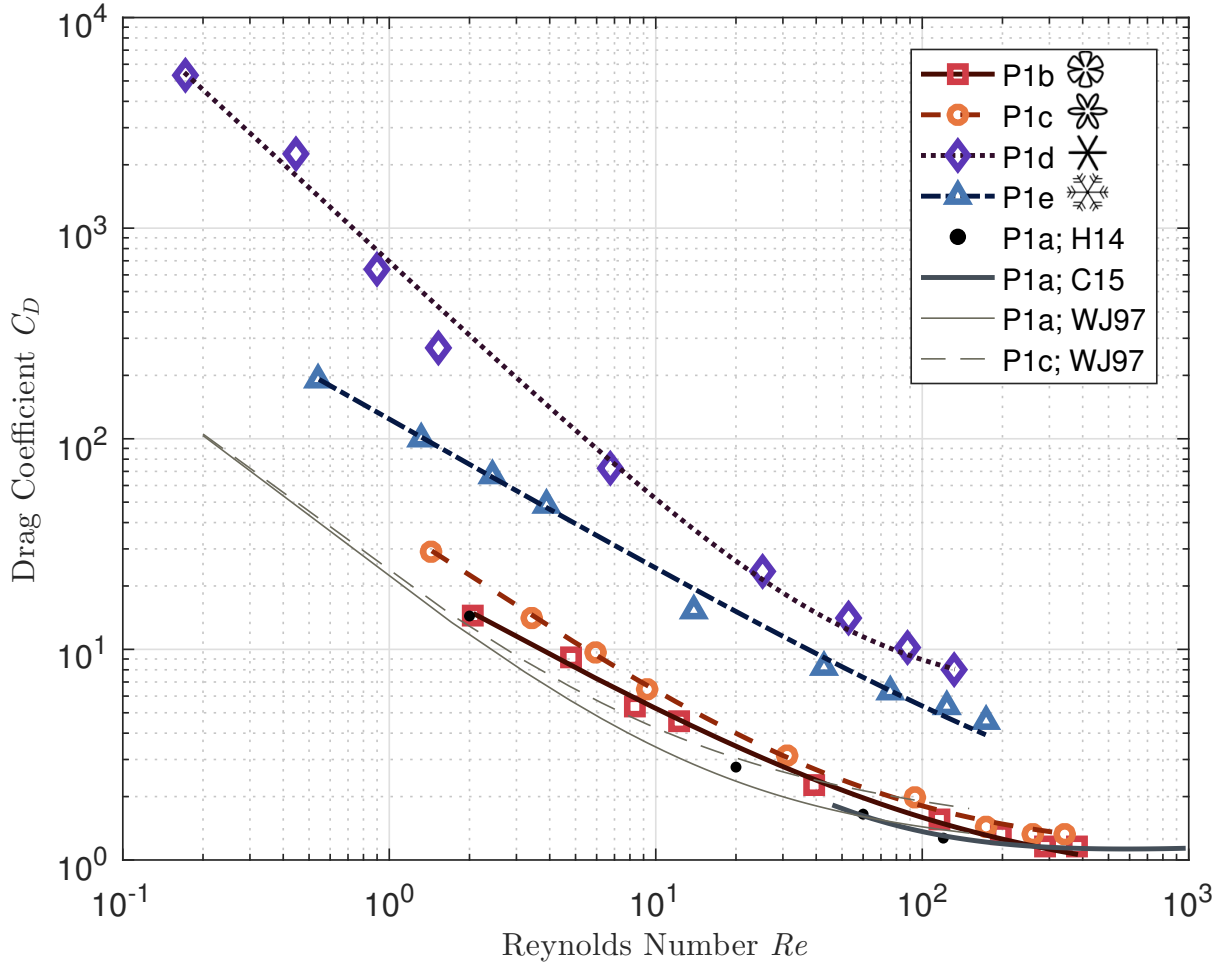
FIGURE 4.14: Drag coefficient of planar crystals. Square, circle, diamond, and triangle markers indicate the results for: sector plates (P1b), broad-branched crystals (P1c), stellar crystal (P1d), and ordinary dendritic crystals (P1e), respectively. The corresponding curves are the power law fits given by Equations (4.6) to (4.9): solid curve for sector plates, dashed curve for broad-branched crystals, dotted curve for sector plates, and dash-dot curve for dendrites. Bolded bullets represent the steady state drag coefficients for hexagonal plates from Hashino et al. (2014). Thick, grey, solid curve represents the parameterization of hexagonal plates from Cheng et al. (2015). The parameterizations of Wang and Ji (1997) are shown in thin lines: solid curve for hexagonal plates, dashed curve for broad-branched crystals.

The drag coefficient for the crystal types in this study can be fit by the following two term power law relationships:

$$\text{Sector plates: } C_D = 23.80\,Re^{-0.7229} + 0.7398, \tag{4.6}$$

$$\text{Broad-branched crystals: } C_D = 38.85\,Re^{-0.8652} + 1.085, \tag{4.7}$$

$$\text{Stellar crystals: } C_D = 686\,Re^{-1.173} + 5.842, \tag{4.8}$$

$$\text{Ordinary Dendritic crystals: } C_D = 123\,Re^{-0.7206} + 0.9325, \tag{4.9}$$

where all variables are dimensionless. The root-mean-square error of the fits are 0.404, 0.193, 179.9, and 1.884, respectively, with adjusted r^2 values of 0.0024, 0.9996, 0.9686, and 0.9991, respectively. Power law relationships were selected, because polynomial fits might over-fit the data and are not representative of a realistic relationship. The relationships are valid over the range of Re corresponding to each crystal type, found in Table 2.3.

4.3 Vapor Density Distribution

The ventilation effect, the enhancement of the diffusional growth/evaporation rate of cloud and precipitation particles due to movement relative to the flow, is due to the enhancement of the vapor density gradient around a falling hydrometeor compared to a stationary one (see Section 2.4).

The computed vapor density distributions in the y-z plane around 5 mm diameter crystals studied are shown in Figure 4.15. In common with all simulations, areas sufficiently

far from the crystals and the upstream region are characterized by high vapor density equal to the environmental 2% supersaturation condition, with lower vapor density in the downstream region. This is caused by the motion of the ice crystals; a stationary crystal in such an environment would have a symmetric vapor density distribution (e.g., Figure 2.6). In the downstream wake, there is an asymmetry in the vapor distribution for the sector plate and broad-branched crystal (Re 384 and 385, respectively), and general symmetry for the stellar and ordinary dendritic crystals (Re 133, 173, respectively). The stronger return flows of the sector plate and broad-branched crystal act to transport the water vapor closer to the surface of the crystal in the wake, leading to a tighter gradient downstream. The vapor distribution is determined by both the convective current ($\rho_v \mathbf{u}$) and the diffusion current ($-D_v \nabla \rho_v$) from (2.27), though the convective current dominates in the case of large $\mathbf{u}$, which explains why the distribution closely resembles the flow field. Important for the diffusional growth of an ice crystal is the gradient of the vapor density, with the largest gradient corresponding to the highest local diffusion rate (Cheng et al., 2014). The highest vapor density gradients are seen upstream of the crystal, though the gradient downstream is certainly not negligible. Note that the patterns shown change with time for unsteady flow, though the patterns and characteristics described above remain similar over time.

The results of the mean ventilation coefficient are summarized in Figure 4.16, and include numerical results from Ji and Wang (1999). The results from the current study can be fit
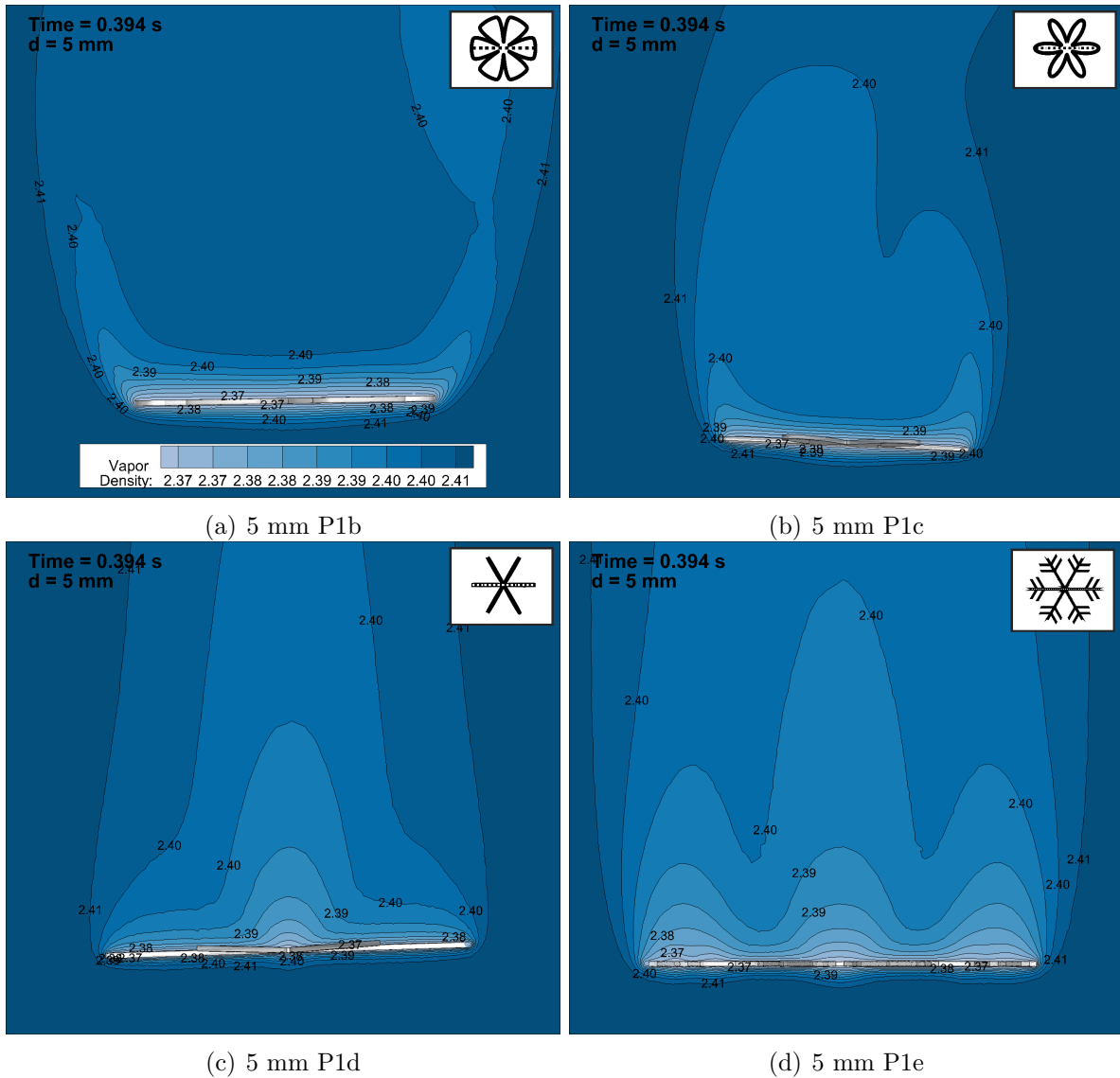
(a) 5 mm P1b

(b) 5 mm P1c

(c) 5 mm P1d

(d) 5 mm P1e

FIGURE 4.15: Vapor density distributions (g m^{-3}) around planar crystals with maximum dimension (diameter) of 5 mm. Vapor density is shown by shades of blue (darker: approaching 2% supersaturation $\rho_v = 2.4086$ g m^{-3}; lighter: approaching saturation $\rho_v = 2.3613$ g m^{-3}). All snapshots correspond to the same randomly selected timestep.

by the following empirical formulae, taking a form similar to that of Ji and Wang (1999):

Sector plates:

$$\bar{f}_v = 1 + 0.9146\,(X/10) + 3.317\,(X/10)^2 \tag{4.10}$$

$$- 2.127\,(X/10)^3 + 0.5171\,(X/10)^4,$$

Broad-branched crystals:

$$\bar{f}_v = 1 + 0.6761\,(X/10) + 3.780\,(X/10)^2 \tag{4.11}$$

$$- 2.518\,(X/10)^3 + 0.5845\,(X/10)^4,$$

Stellar crystals:

$$\bar{f}_v = 1 - 0.0440\,(X/10) + 7.915\,(X/10)^2 \tag{4.12}$$

$$- 7.778\,(X/10)^3 + 2.4040\,(X/10)^4,$$

Ordinary dendritic crystals:

$$\bar{f}_v = 1 + 0.2834\,(X/10) + 6.066\,(X/10)^2 \tag{4.13}$$

$$- 1.612\,(X/10)^3 - 0.5295\,(X/10)^4,$$

where $\bar{f}_v$ is the dimensionless ventilation coefficient and X is a dimensionless number defined as

$$X = (N_{Scv})^{1/3}\,(Re)^{1/2}, \tag{4.14}$$

where N_{Scv} is the Schmidt number of water vapor $\left(^{\mathrm{N}_{Sc}\ \text{air kinematic viscosity}}/_{\mathrm{N}_{Sc}\ \text{water vapor diffusivity}}\right)$.

The functional dependence of $\bar{f}_v$ on X has been found by Pitter et al. (e.g. 1974). As in Ji and Wang (1999), N_{Scv} is held at a constant value (=0.63), so the relationships

in Equations (4.10) to (4.13) are essentially between $\bar{f}_v$ and Re. The root-mean-square

errors for the above relationships are 0.034, 0.018, 0.014, and 0.028, respectively, and are

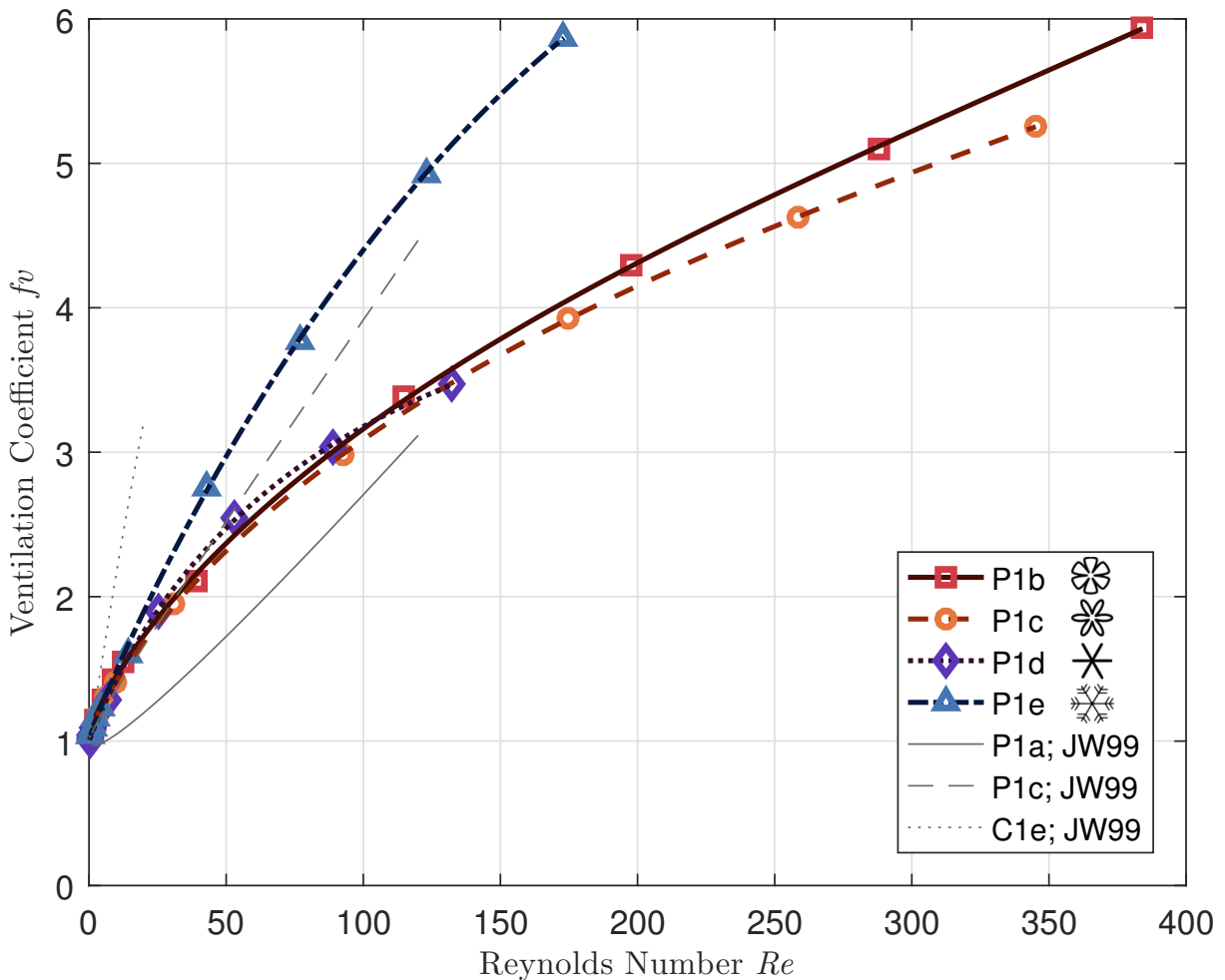valid over the range of Re corresponding to each crystal type, found in Table 2.3.

FIGURE 4.16: Ventilation coefficient of planar crystals. Square, circle, diamond, and triangle markers indicate the results for: sector plates (P1b), broad-branched crystals (P1c), stellar crystals (P1d), and ordinary dendritic crystals (P1e), respectively. The corresponding curves are the power law fits given by Equations (4.10) to (4.13): solid curve for sector plates, dashed curve for broad-branched crystals, dotted curve for sector plates, and dash-dot curve for dendrites. The parameterizations of Ji and Wang (1999) are shown in thin lines: dotted curve for circular columns, solid curve for hexagonal plates, dashed curve for broad-branched crystals.

Figure 4.16 also shows that the ordinary dendritic crystals generally have the higher ventilation coefficient, at a given Reynolds number, compared to the other crystal habits. This becomes more pronounced with increasing Re. This can be understood by considering the dimensions and structure of the varying crystal habits. The more skeletal structure of a dendrite allows for a greater surface area that can be subjected to the ventilation effect, despite falling at a lower terminal velocity compared to the sector plate and broad-branched crystal at the same Re.

Chapter 5

Summary

The numerical simulations of the hydrodynamic behavior of four types of freely falling planar ice crystals are performed in this study. The crystals range from 0.2 mm – 0.5 mm, and 1 mm – 5 mm in maximum diameter, and cover both steady and unsteady flow regimes. Fall behavior, flow characteristics, and an analysis of the results are reported, and are in general agreement with previous numerical studies and reported observations. Allowing the crystals to respond to the forcing of the flow field, as first done in Cheng et al. (2015) for a hexagonal plate, provides for more realistic results and works to improve the understanding of frozen precipitation particles in clouds. These results can be parameterized for use by cloud and numerical weather prediction models. One particularly interesting question: given ventilation coefficients for low-to-intermediate Reynolds numbers in this study, can downbursts be more realistically numerically simulated?

Only idealized, symmetric crystals are simulated. Observations show that natural ice crystals do not demonstrate near-perfect symmetry most of the time, and often have rough surfaces. Simulations can easily be run for different environmental conditions (temperature and pressure) for comparison. Additionally, individual ice crystals often form aggregates with other crystals while they fall toward the surface of the earth. Simulating the flow fields around crystal aggregates is the next phase of this study. This endeavor will prove more challenging to mesh and simulate, though early trials from a colleague in the lab are promising.

Bibliography

Abraham, F. F., 1970: Functional Dependence of Drag Coefficient of a Sphere on Reynolds Number. *Physics of Fluids (1958-1988)*, **13**, 2194–2195, doi:10.1063/1.1693218.

ANSYS, 2013: ANSYS Release 15.0 Fluent Theory Guide. Tech. Rep., ANSYS, Inc.

Auer, A. H. and D. L. Veal, 1970: The Dimension of Ice Crystals in Natural Clouds. *J. Atmos. Sci.*, **27**, 919–926, doi:10.1175/1520-0469(1970)027<0919:TDOICI>2.0.CO;2.

Beard, K. V., 1980: The Effects of Altitude and Electrical Force on the Terminal Velocity of Hydrometeors. *J. Atmos. Sci.*, **37**, 1363–1374, doi:10.1175/1520-0469(1980)037<1363:TEOAAE>2.0.CO;2.

Brutsaert, W., 1982: *Evaporation into the Atmosphere*. Springer, Dordrecht.

Böhm, H. P., 1989: A General Equation for the Terminal Fall Speed of Solid Hydrometeors. *J. Atmos. Sci.*, **46**, 2419–2427, doi:10.1175/1520-0469(1989)046<2419:AGEFTT>2.0.CO;2.

Cheng, K.-Y., P. K. Wang, and T. Hashino, 2015: A Numerical Study on the Attitudes and Aerodynamics of Freely Falling Hexagonal Ice Plates. *J. Atmos. Sci.*, doi:10.1175/JAS-D-15-0059.1.

Cheng, K.-Y., P. K. Wang, and C.-K. Wang, 2014: A Numerical Study on the Ventilation Coefficients of Falling Hailstones. *J. Atmos. Sci.*, **71**, 2625–2634, doi:10.1175/JAS-D-13-0229.1.

Cornford, S. G., 1965: Fall speeds of precipitation elements. *Q.J.R. Meteorol. Soc.*, **91**, 91–94, doi:10.1002/qj.49709138713.

Dennis, S. C. R. and G.-Z. Chang, 1969: Numerical Integration of the Navier–Stokes Equations for Steady Two–Dimensional Flow. *Physics of Fluids (1958-1988)*, **12**, II–88–II–93, doi:10.1063/1.1692474.

Diedenhoven, B. v., B. Cairns, I. V. Geogdzhayev, A. M. Fridlind, A. S. Ackerman, P. Yang, and B. A. Baum, 2012: Remote sensing of ice crystal asymmetry parameter using multi-directional polarization measurements - Part 1: Methodology and evaluation with simulated measurements. *ResearchGate*, **5**, 2361–2374, doi:10.5194/amt-5-2361-2012.

Dixon, J. C., 2007: Appendix B: Properties of Air. *The Shock Absorber Handbook*, John Wiley & Sons, Ltd, 375–378.

Field, S. B. and M. Klaus, 1997: Chaotic dynamics of falling disks. *Nature*, **388**, 252.

Freitas, C. J., R. L. Street, A. N. Findikakis, and J. R. Koseff, 1985: Numerical simulation of three-dimensional flow in a cavity. *Int. J. Numer. Meth. Fluids*, **5**, 561–575, doi:10.1002/fld.1650050606.

Gravner, J. and D. Griffeath, 2009: Modeling snow-crystal growth: A three-dimensional mesoscopic approach. *Phys. Rev. E*, **79**, 011601, doi:10.1103/PhysRevE.79.011601.

Hall, W. D. and H. R. Pruppacher, 1976: The Survival of Ice Particles Falling from Cirrus Clouds in Subsaturated Air. *J. Atmos. Sci.*, **33**, 1995–2006, doi:10.1175/1520-0469(1976)033<1995:TSOIPF>2.0.CO;2.

Hallett, J., 1965: Field and Laboratory Observations of Ice Crystal Growth from the Vapor. *J. Atmos. Sci.*, **22**, 64–69, doi:10.1175/1520-0469(1965)022<0064:FALOOI>2.0.CO;2.

Hashino, T., K.-Y. Cheng, C.-C. Chueh, and P. K. Wang, 2016: Numerical Study of Motion and Stability of Falling Columnar Crystals. *J. Atmos. Sci.*, **73**, 1923–1942, doi:10.1175/JAS-D-15-0219.1.

Hashino, T., M. Chiruta, D. Polzin, A. Kubicek, and P. K. Wang, 2014: Numerical simulation of the flow fields around falling ice crystals with inclined orientation and the hydrodynamic torque. *Atmospheric Research*, **150**, 79–96, doi:10.1016/j.atmosres.2014.07.003.

Heymsfield, A., 1972: Ice Crystal Terminal Velocities. *J. Atmos. Sci.*, **29**, 1348–1357, doi:10.1175/1520-0469(1972)029<1348:ICTV>2.0.CO;2.

Heymsfield, A. J., A. Bansemer, and C. H. Twohy, 2007a: Refinements to Ice Particle Mass Dimensional and Terminal Velocity Relationships for Ice Clouds. Part I: Temperature Dependence. *J. Atmos. Sci.*, **64**, 1047–1067, doi:10.1175/JAS3890.1.

Heymsfield, A. J. and M. Kajikawa, 1987: An Improved Approach to Calculating Terminal Velocities of Plate-like Crystals and Graupel. *J. Atmos. Sci.*, **44**, 1088–1099, doi:10.1175/1520-0469(1987)044<1088:AIATCT>2.0.CO;2.

Heymsfield, A. J., G.-J. van Zadelhoff, D. P. Donovan, F. Fabry, R. J. Hogan, and A. J. Illingworth, 2007b: Refinements to Ice Particle Mass Dimensional and Terminal Velocity Relationships for Ice Clouds. Part II: Evaluation and Parameterizations of Ensemble Ice Particle Sedimentation Velocities. *J. Atmos. Sci.*, **64**, 1068–1088, doi:10.1175/JAS3900.1.

Heymsfield, A. J. and C. D. Westbrook, 2010: Advances in the Estimation of Ice Particle Fall Speeds Using Laboratory and Field Measurements. *J. Atmos. Sci.*, **67**, 2469–2482, doi:10.1175/2010JAS3379.1.

Higuchi, K., 1956: New method for the simultaneous observation of shape and size of a large number of falling snow particles. *J. Meteor.*, **13**, 274–278, doi:10.1175/1520-0469(1956)013<0274:NMFTSO>2.0.CO;2.

Hobbs, P. V., S. Chang, and J. D. Locatelli, 1974: The dimensions and aggregation of ice crystals in natural clouds. *J. Geophys. Res.*, **79**, 2199–2206, doi:10.1029/JC079i015p02199.

Ishimoto, H., 2008: Radar Backscattering Computations for Fractal-Shaped Snowflakes. *ResearchGate*, **86**, 459–469, doi:10.2151/jmsj.86.459.

Issa, R. I., 1986: Solution of the implicitly discretised fluid flow equations by operator-splitting. *Journal of Computational Physics*, **62**, 40–65, doi:10.1016/0021-9991(86)90099-9.

Jayaweera, K. O. L. F., 1972: An Equivalent Disc for Calculating the Terminal Velocities of Plate-Like Ice Crystals. *J. Atmos. Sci.*, **29**, 596–598, doi:10.1175/1520-0469(1972)029<0596:AEDFCT>2.0.CO;2.

Jayaweera, K. O. L. F. and R. E. Cottis, 1969: Fall velocities of plate-like and columnar ice crystals. *Q.J.R. Meteorol. Soc.*, **95**, 703–709, doi:10.1002/qj.49709540604.

Jayaweera, K. O. L. F. and B. J. Mason, 1965: The behaviour of freely falling cylinders and cones in a viscous fluid. *Journal of Fluid Mechanics*, **22**, 709–720, doi:10.1017/S002211206500109X.

— 1966: The falling motions of loaded cylinders and discs simulating snow crystals. *Q.J.R. Meteorol. Soc.*, **92**, 151–156, doi:10.1002/qj.49709239115.

Jayaweera, K. O. L. F. and B. F. Ryan, 1972: Terminal velocities of ice crystals. *Q.J.R. Meteorol. Soc.*, **98**, 193–197, doi:10.1002/qj.49709841516.

Ji, W. and P. K. Wang, 1990: Numerical simulation of three-dimensional unsteady viscous flow past fixed hexagonal ice crystals in the air — preliminary results. *Atmospheric Research*, **25**, 539–557, doi:10.1016/0169-8095(90)90037-D.

— 1991: Numerical simulation of three-dimensional unsteady viscous flow past finite cylinders in an unbounded fluid at low intermediate reynolds numbers. *Theoret. Comput. Fluid Dynamics*, **3**, 43–59, doi:10.1007/BF00271515.

— 1999: Ventilation Coefficients for Falling Ice Crystals in the Atmosphere at Low–Intermediate Reynolds Numbers. *J. Atmos. Sci.*, **56**, 829–836, doi:10.1175/1520-0469(1999)056<0829:VCFFIC>2.0.CO;2.

Jiusto, J. E. and G. E. Bosworth, 1971: Fall Velocity of Snowflakes. *J. Appl. Meteor.*, **10**, 1352–1354, doi:10.1175/1520-0450(1971)010<1352:FVOS>2.0.CO;2.

Kajikawa, M., 1971: A Model Experimental Study on the Falling Velocity of Ice Crystals. *Journal of the Meteorological Society of Japan. Ser. II*, **49**, 367–375.

— 1972: Measurement of Falling Velocity of Individual Snow Crystals. *Journal of the Meteorological Society of Japan. Ser. II*, **50**, 577–584.

— 1973: Laboratory Measurement of Falling Velocity of Individual Ice crystals. *Journal of the Meteorological Society of Japan. Ser. II*, **51**, 263–272.

— 1992: Observations of the Falling Motion of Plate-Like Snow Crystals Part I: The Free-Fall Patterns and Velocity. *Journal of the Meteorological Society of Japan. Ser. II*, **70**, 1–9.

Kawaguti, M., 1953: Numerical Solution of the Navier-Stokes Equations for the Flow around a Circular Cylinder at Reynolds Number 40. *Journal of the Physical Society of Japan*, **8**, 747–757, doi:10.1143/JPSJ.8.747.

Khvorostyanov, V. I. and J. A. Curry, 2002: Terminal Velocities of Droplets and Crystals: Power Laws with Continuous Parameters over the Size Spectrum. *J. Atmos. Sci.*, **59**, 1872–1884, doi:10.1175/1520-0469(2002)059<1872:TVODAC>2.0.CO;2.

— 2005: Fall Velocities of Hydrometeors in the Atmosphere: Refinements to a Continuous Analytical Power Law. *J. Atmos. Sci.*, **62**, 4343–4357, doi:10.1175/JAS3622.1.

Kikuchi, K., T. Kameda, K. Higuchi, and A. Yamashita, 2013: A global classification of snow crystals, ice crystals, and solid precipitation based on observations from middle latitudes to polar regions. *Atmospheric Research*, **132–133**, 460–472, doi:10.1016/j.atmosres.2013.06.006.

Knight, N. C. and A. J. Heymsfield, 1983: Measurement and Interpretation of Hailstone Density and Terminal Velocity. *J. Atmos. Sci.*, **40**, 1510–1516, doi:10.1175/1520-0469(1983)040<1510:MAIOHD>2.0.CO;2.

Langleben, M. P., 1954: The terminal velocity of snowflakes. *Q.J.R. Meteorol. Soc.*, **80**, 174–181, doi:10.1002/qj.49708034404.

Lim, S., D. Moisseev, V. Chandrasekar, and D.-R. Lee, 2013: Classification and Quantification of Snow Based on Spatial Variability of Radar Reflectivity. *Journal of the Meteorological Society of Japan. Ser. II*, **91**, 763–774, doi:10.2151/jmsj.2013-603.

Liou, K. N., 1992: *Radiation and Cloud Processes in the Atmosphere*. Oxford University Press.

List, R. and R. S. Schemenauer, 1971: Free-Fall Behavior of Planar Snow Crystals, Conical Graupel and Small Hail. *J. Atmos. Sci.*, **28**, 110–115, doi:10.1175/1520-0469(1971)028<0110:FFBOPS>2.0.CO;2.

Liu, H.-C., P. K. Wang, and R. E. Schlesinger, 2003: A Numerical Study of Cirrus Clouds. Part I: Model Description. *J. Atmos. Sci.*, **60**, 1075–1084, doi:10.1175/1520-0469(2003)60<1075:ANSOCC>2.0.CO;2.

Locatelli, J. D. and P. V. Hobbs, 1974: Fall speeds and masses of solid precipitation particles. *J. Geophys. Res.*, **79**, 2185–2197, doi:10.1029/JC079i015p02185.

Magono, C., 1954: On the Falling Velocity of Solid Precipitation Elements. *Sci. Repts. Yokohama Natl. Univ., Sect. 1,*, **3**, 33–40.

Magono, C. and C. W. Lee, 1966: Meteorological Classification of Natural Snow Crystals. *J. Fac. Sci., Hokkaido Univ., Ser 7*, **2**, 321–335.

Marshall, J. S., 1953: Precipitation trajectories and patterns. *J. Meteor.*, **10**, 25–29, doi:10.1175/1520-0469(1953)010<0025:PTAP>2.0.CO;2.

Masliyah, J. H. and N. Epstein, 1970: Numerical study of steady flow past spheroids. *Journal of Fluid Mechanics*, **44**, 493–512, doi:10.1017/S0022112070001957.

Mason, B. J., 1953: The growth of ice crystals in a supercooled water cloud. *Q.J.R. Meteorol. Soc.*, **79**, 104–111, doi:10.1002/qj.49707933909.

— 1971: *The Physics of Clouds*, volume 98. Oxford University Press, 2 edition.

Matrosov, S. Y., 2007: Modeling Backscatter Properties of Snowfall at Millimeter Wavelengths. *J. Atmos. Sci.*, **64**, 1727–1736, doi:10.1175/JAS3904.1.

Matrosov, S. Y., R. F. Reinking, and I. V. Djalalova, 2005: Inferring Fall Attitudes of Pristine Dendritic Crystals from Polarimetric Radar Data. *J. Atmos. Sci.*, **62**, 241–250, doi:10.1175/JAS-3356.1.

Michaeli, G., 1977: Settling velocities of small ice crystals. *Tellus*, **29**, 282–285, doi:10.1111/j.2153-3490.1977.tb00737.x.

Mitchell, D. L., 1996: Use of Mass- and Area-Dimensional Power Laws for Determining Precipitation Particle Terminal Velocities. *J. Atmos. Sci.*, **53**, 1710–1723, doi:10.1175/1520-0469(1996)053<1710:UOMAAD>2.0.CO;2.

Mitchell, D. L. and A. J. Heymsfield, 2005: Refinements in the Treatment of Ice Particle Terminal Velocities, Highlighting Aggregates. *J. Atmos. Sci.*, **62**, 1637–1644, doi:10.1175/JAS3413.1.

Nakaya, U. and Y. Sekido, 1936: General Classification of Snow Crystals and their Frequency of Occurrence. *J. Fac. Sci., Hokkaido Univ., Ser 2*, **1**, 243–264.

Nakaya, U. and T. J. Terada, 1935: Simultaneous Observations of the Mass, Falling Velocity and Form of Individual Snow Crystals. *J. Fac. Sci. Hokkaido Imp. Univ.*, **1**.

Nieuwstadt, F. and H. B. Keller, 1973: Viscous flow past circular cylinders. *Computers & Fluids*, **1**, 59–71, doi:10.1016/0045-7930(73)90026-1.

Ono, A., 1969: The Shape and Riming Properties of Ice Crystals in Natural Clouds. *J. Atmos. Sci.*, **26**, 138–147, doi:10.1175/1520-0469(1969)026<0138:TSARPO>2.0.CO;2.

— 1970: Growth Mode of Ice Crystals in Natural Clouds. *J. Atmos. Sci.*, **27**, 649–658, doi:10.1175/1520-0469(1970)027<0649:GMOICI>2.0.CO;2.

Pitter, R. L. and H. R. Pruppacher, 1974: A Numerical Investigation of Collision Efficiencies of Simple Ice Plates Colliding With Supercooled Water Drops. *J. Atmos. Sci.*, **31**, 551–559, doi:10.1175/1520-0469(1974)031<0551:ANIOCE>2.0.CO;2.

Pitter, R. L., H. R. Pruppacher, and A. E. Hamielec, 1973: A Numerical Study of Viscous Flow Past a Thin Oblate Spheroid at Low and Intermediate Reynolds Numbers. *J. Atmos. Sci.*, **30**, 125–134, doi:10.1175/1520-0469(1973)030<0125:ANSOVF>2.0.CO;2.

— 1974: A Numerical Study of the Effect of Forced Convection on Mass Transport from a Thin Oblate Spheroid of Ice in Air. *J. Atmos. Sci.*, **31**, 1058–1066, doi:10.1175/1520-0469(1974)031<1058:ANSOTE>2.0.CO;2.

Pruppacher, H. R. and J. D. Klett, 1997: *Microphysics of Clouds and Precipitation*. Kluwer Academic Publishers, 2nd edition.

Rimon, Y. and H. J. Lugt, 1969: Laminar Flows Past Oblate Spheroids of Various Thicknesses. *Physics of Fluids (1958-1988)*, **12**, 2465–2472, doi:10.1063/1.1692382.

Sasyo, Y., 1971: Study of the Formation of Precipitation by the Aggregation of Snow Particles and the Accretion of Cloud Droplets on Snowflakes. *Papers in Meteorology and Geophysics*, **22**, 69–142, doi:10.2467/mripapers1950.22.2-69.

Schaefer, V. J., 1947: Properties of particles of snow and the electrical effects they produce in storms. *Eos Trans. AGU*, **28**, 587–614, doi:10.1029/TR028i004p00587.

Schlamp, R. J., H. R. Pruppacher, and A. E. Hamielec, 1975: A Numerical Investigation of the Efficiency with which Simple Columnar Ice Crystals Collide with Supercooled Water Drops. *J. Atmos. Sci.*, **32**, 2330–2337, doi:10.1175/1520-0469(1975)032<2330:ANIOTE>2.0.CO;2.

Starr, D. O. and S. K. Cox, 1985: Cirrus Clouds. Part I: A Cirrus Cloud Model. *ResearchGate*, **42**, 2663–2681, doi:10.1175/1520-0469(1985)042<2663:CCPIAC>2.0.CO;2.

Stringham, G., D. Simons, and H. Guy, 1969: The behavior of large particles falling in quiescent liquids. USGS Numbered Series 562-C.

Takahashi, T., 2014: Influence of Liquid Water Content and Temperature on the Form and Growth of Branched Planar Snow Crystals in a Cloud. *J. Atmos. Sci.*, **71**, 4127–4142, doi:10.1175/JAS-D-14-0043.1.

Takano, Y. and K. N. Liou, 1993: Transfer of polarized infrared radiation in optically anisotropic media: application to horizontally oriented ice crystals. *J. Opt. Soc. Am. A,*, **10**, 1243–1256, doi:10.1364/JOSAA.10.001243.

Thom, A., 1933: The Flow Past Circular Cylinders at Low Speeds. *Proceedings of the Royal Society of London A: Mathematical, Physical and Engineering Sciences*, **141**, 651–669, doi:10.1098/rspa.1933.0146.

Vittori, O. A. and V. Prodi, 1967: Scavenging of Atmospheric Particles by Ice Crystals. *J. Atmos. Sci.*, **24**, 533–538, doi:10.1175/1520-0469(1967)024<0533:SOAPBI>2.0.CO;2.

Wang, P. K., 1982: Mathematical Description of the Shape of Conical Hydrometeors. *J. Atmos. Sci.*, **39**, 2615–2622, doi:10.1175/1520-0469(1982)039<2615:MDOTSO>2.0.CO;2.

— 1987: Two-dimensional shape and size characterization of polygonally symmetric particles. *Journal of Colloid and Interface Science*, **117**, 271–281, doi:10.1016/0021-9797(87)90191-3.

— 1997: Characterization of Ice Crystals in Clouds by Simple Mathematical Expressions Based on Successive Modification of Simple Shapes. *J. Atmos. Sci.*, **54**, 2035–2041, doi:10.1175/1520-0469(1997)054<2035:COICIC>2.0.CO;2.

— 1999: Three-Dimensional Representations of Hexagonal Ice Crystals and Hail Particles of Elliptical Cross Sections. *J. Atmos. Sci.*, **56**, 1089–1093, doi:10.1175/1520-0469(1999)056<1089:TDROHI>2.0.CO;2.

— 2013: *Physics and Dynamics of Clouds and Precipitation*. Cambridge University Press.

Wang, P. K. and S. M. Denzer, 1983: Mathematical Description of the Shape of Plane Hexagonal Snow Crystals. *J. Atmos. Sci.*, **40**, 1024–1028, doi:10.1175/1520-0469(1983)040<1024:MDOTSO>2.0.CO;2.

Wang, P. K. and W. Ji, 1997: Numerical Simulation of Three-Dimensional Unsteady Flow past Ice Crystals. *J. Atmos. Sci.*, **54**, 2261–2274, doi:10.1175/1520-0469(1997)054<2261:NSOTDU>2.0.CO;2.

— 2000: Collision Efficiencies of Ice Crystals at Low–Intermediate Reynolds Numbers Colliding with Supercooled Cloud Droplets: A Numerical Study. *J. Atmos. Sci.*, **57**, 1001–1009, doi:10.1175/1520-0469(2000)057<1001:CEOICA>2.0.CO;2.

Willmarth, W., N. Hawk, and R. Harvey, 1964: Steady and Unsteady Motions and Wakes of Freely Falling Disks. *Phys. Fluids*, **7**, 197, doi:10.1063/1.1711133.

Yau, M. K. and R. R. Rogers, 1996: *A Short Course in Cloud Physics*. Elsevier Science, Saint Louis, 3 edition.

Young, K. C., 1993: *Microphysical Processes in Clouds*. Oxford University Press, New York.

Zikmunda, J. and G. Vali, 1972: Fall Patterns and Fall Velocities of Rimed Ice Crystals. *J. Atmos. Sci.*, **29**, 1334–1347, doi:10.1175/1520-0469(1972)029<1334:FPAFVO>2.0.CO;2.